https://doi.org/10.5194/ar-2023-14
Preprint. Discussion started: 3 November 2023

AEROSOL Research Discussions

On Formation of Carbonaceous Impurities in Flame Spray Synthesis of Maghemite Nanoparticles

Ricardo Tischendorf[1], Kristina Duschik[2], Sophie Dupont[3], Fabian Fröde[4], Heinz Pitsch[4], Reinhold Kneer[3], Mirko Schaper[2], Hans-Joachim Schmid[1].

[1]Particle Technology Group, University of Paderborn, 33102 Paderborn, Germany
[2]Department of Material Science, University of Paderborn, 33100 Paderborn, Germany
[3]Institute of Heat and Mass Transfer, RWTH Aachen, 52056 Aachen, Germany
[4]Institute for Combustion Technology, RWTH Aachen, 52056 Aachen, Germany

Correspondence to: Ricardo Tischendorf (Ricardo.Tischendorf@upb.de)

Abstract

Particles generated by spray flame synthesis (SFS) can exhibit impurities, with surface adsorbates and soot being the best-known examples. Unfortunately, the extent to which the formation of these impurities can be characterized, and how their formation can be avoided is not fully understood yet. In order to contribute to the understanding of the formation of carbonaceous impurities, we investigated their formation using a standardized burner type (SpraySyn burner) while synthesizing maghemite by the gas-to-particle conversion. Two approaches were followed to characterize the formation of soot and surface adsorbates in this paper. Firstly, fabricated powders were analyzed by complementary powder analysis. In this term, the detection of soot was negative, but powders contained carboxylates and carbonates, which were bound to particle surfaces. The methodological procedure used allowed a reliable quantification of those adsorbates, and it was possible to normalize their relative mass fractions (up to ~16%) to the powders' respective specific surface areas. The normalization approach yielded a surface loading values of 0.84-0.85 mg m^{-2}. The methodical procedure and the data provided can be used in the future to denote/compare SFS materials in sensitivity studies. Secondly, particles were thermophoretically extracted from the process in situ and subsequently characterized by transmission electron microscopy (TS-TEM). Interestingly, particles extracted at 5 cm height above the burner (HAB) (representing the center of the visible flame) showed amorphous core-shell structures and amorphous aggregates, indicating a coexistence of soot alongside maghemite particles. Via reducing the sampling time of the TS system to 1.5 ms samples were taken either from flame pulses (a state of high flame activity) or from flame flickering (lower flame activity). A comparison of these samples showed that heterogeneous particle structures formed predominantly in flame pulses. As samples extracted at 15 cm HAB neither showed amorphous coating nor amorphous aggregates, it was indicated that soot fractions oxidize between 5 and 15 cm HAB.

https://doi.org/10.5194/ar-2023-14
Preprint. Discussion started: 3 November 2023

AEROSOL Research Discussions

1 Introduction

Spray flame synthesis (SFS) is a versatile technique for fabricating a wide range of materials, including nanoparticulate iron oxides (Fe_xO_y) with great potential for various engineering applications (Li et al. 2016; Strobel und Pratsinis 2007; Teoh et al. 2010). For example, superparamagnetic maghemite and magnetite particles derived from SFS can be utilized in medical hyperthermia, drug delivery, and protein separation due to their magnetic properties (Huber 2005; Herrmann et al. 2009; Pankhurst et al. 2003; Gupta und Gupta 2005; Majewski und Thierry 2007; Gul et al. 2019). In SFS, a liquid combustible precursor solution is atomized into a self-sustaining flame (pilot flame) through a nozzle. The resulting spray ignites, and forms a turbulent, reactive multiphase flow field in which particles can evolve through two distinct pathways. On the one hand, particles are generated by the gas-to-particle pathway from gas borne product molecules via nucleation, agglomeration, growth and sintering in the gas phase. On the other hand, particles are formed via the droplet-to-particle pathway implying a precursor precipitation or reaction within the liquid phase (Teoh et al. 2010). In most cases all particles formed in one droplet will agglomerate upon evaporation of the solvent followed by sintering. Therefore, particles formed by the droplet pathway are typically much larger compared to particles generated via the gas-to-particle pathway. As several particulate functional properties depend on the particles disperse characteristics, the dominance of the pathways critically affects the potential material application. For example, the crystallite size, and the oxidation state greatly influence the magnetic saturation of superparamagnetic iron oxides (Li et al. 2007; Chatterjee et al. 2003). However, also the powder purity (presence of non-product species) critically alters the application. For instance in terms of iron oxides, superparamagnetic properties are also altered by surface chemistry/purity (Sodipo und Aziz 2016). Having the relevance of powder purity in mind, some experimental parameter studies have been carried out in the past decades, where it was addressed to what extent iron-based materials can be prepared with certain purity.

Organic species can attach to particle surfaces, representing an important contamination type. For example, Grimm et al. produced maghemite particles by atomizing either iron pentacarbonyl or iron (III) acetylacetonate in toluene (Grimm et al. 1997a; Grimm et al. 1997b), and the authors investigated powder purities by means of Fourier Transform Infrared Spectroscopy (FTIR) and Thermogravimetric analysis (TGA). In their study they concluded that CO_2 was bound to the particle surfaces, which contributed up to ~2% of the total powder mass. More recent FTIR measurements, e.g., as conducted by Alkan et al. and Meierhofer et al., have shown that much more complex species than CO_2 can also bind to particle surfaces (Alkan et al. 2020; Meierhofer et al. 2017). In their studies, the authors used SFS to prepare titanium- and iron-based materials, such as $LaCo_{1-x}Fe_xO_3$ perovskite, and the presence of surface-bound carbonates (CO_3^{2-}) and carboxylates ($R\text{-}COO^-$) was revealed. It is well-known from wet-phase chemistry that carbonates and carboxylates can bind on iron oxide surfaces. In a recent study Carvajal et al. have shown that nitrogenous species can also be present as impurities in SFS prepared iron oxide powders (Carvajal et al. 2020) in case iron (III) nitrate (INN) is used as a precursor. The authors identified the presence of nitrogen by coupling TGA measurements to Mass Spectroscopy, and stated that NO_x species were attached on particle surfaces.

https://doi.org/10.5194/ar-2023-14
Preprint. Discussion started: 3 November 2023

In addition to surface-bound adsorbates, elemental carbon (usually also referred to as graphite or soot) is another possible impurity. It can either deposit as an amorphous layer on product particle surfaces, but can also form independent, amorphous particles. In a study from Strobel et al. it was shown that graphite formation can be significantly influenced in certain SFS setups by adapting the global oxygen stoichiometry (Φ) (Strobel und Pratsinis 2009). For this purpose, the authors used a closed combustion chamber. The generated particles were studied by Raman spectroscopy, transmission electron microscopy (TEM), and X-ray powder diffraction (XRD). Their experiment showed that carbon was formed significantly at oxygen restriction Φ >0.98. Thus, from this study it was indicated that a soot formation can be easily avoided using global oxygen excess. However, as meanwhile shown by Carvajal et al. amorphous carbon can also form at high excess oxygen (Carvajal et al. 2020). As shown in their study by TEM imaging, produced iron oxide were covered by carbon coatings with a few nanometres of thickness. And during TGA-MS their samples showed high relative mass losses during heating (double-digit %range). At first glance the study by Carvajal et al. appears to be contradictory to the study of Strobel et al. However, the contradiction may be probably explained as different burner setups and precursor compositions were utilized in those studies. Although elemental carbon can represent a impurity in FSP, it is noteworthy that carbon encapsulated iron oxides were also prepared with manufacturer intension in the past. E.g., as presented by Li et al. and Herrman et al., carbon coatings can be beneficial since they can prevent reduced iron oxide phases against oxidation (Li et al. 2013; Herrmann et al. 2009).

This very brief comparison of literature data shows quite different results in terms of formation of organic and inorganic impurities in the SFS of iron-based materials. However, the differences in the literature data are by no means contradictory. Instead, they are merely the result of the high degree of freedom that SFS offers. Hence, most studies used different burner types, material systems, and precursor compositions, limiting the comparability of studies drastically. Therefore, it seems to be beneficial in the future to develop and establish standardized SFS experiments for the characterization of product impurities. For this purpose, standardized burner types as well as standardized precursor mixtures are necessary. Having such standard procedures will then allow to perform fundamental studies to thoroughly investigate the mechanisms and specific conditions controlling the formation of such impurities.

For the synthesis of iron oxides, a standard SFS setup was proposed in 2019 by Schneider et al. (Schneider et al. 2019). In this publication, the so-called SpraySyn burner was presented, which established subsequently for laboratory experiments (Aßmann et al. 2020, 2021; Bierwirth et al. 2021; Foo et al. 2022; Kumar et al. 2023; Li et al. 2021; Martins et al. 2020; Prenting et al. 2020; Prenting et al. 2021; Rahinov et al. 2020) and numerical investigations (Abdelsamie et al. 2021; Abdelsamie et al. 2020; Abdelsamie und Thévenin 2019; Kirchmann et al. 2021; Kotalczyk et al. 2019, 2022; Martins et al. 2021; Nanjaiah et al. 2021; Saber et al. 2022; Sellmann et al. 2022; Skenderović et al. 2018; Wollny et al. 2020). By using the SpraySyn burner and INN dissolved in Ethanol (EtOH) and 2-ethylhexanoic acid (2-EHA) as precursor composition, particles predominately evolve by the gas-to-particle conversion making this setup a promising reference setup. Although this particular setup has already been used in some experimental approaches, it was not systematically investigated for the formation of impurities until now. To fill this gap, we characterized the formation of impurities, namely soot and surface adsorbates, using two complementary approaches. In the first approach, we comprehensively investigated final powder products using offline

https://doi.org/10.5194/ar-2023-14
Preprint. Discussion started: 3 November 2023

powder analysis. For this purpose, powder samples were generated using different precursor concentrations. In the second approach, we used thermophoretic sampling (TS) to extract particle samples from the process in-situ which were subsequently analysed by TEM (TS-TEM). For this latter approach, a new TS probe was constructed and evaluated in our laboratory. As several technical aspects must be taken into account in designing TS probing systems, we performed a brief literature study concerning the development of TS probes in past decades. Hence, this publication also reflects some aspects in the history in probe TS design. Noteworthy, it is well known that TS-TEM established as standard-technique for probing from aerosols. However, it was dominantly applied for sampling from laminar diffusion flames, and reports which utilized TS-TEM for SFS processes are still rare. Hence, we also address special issues which have to be taken into account for TS-TEM sampling from SFS.

2 Material and methods

In this chapter most important information necessary to reproduce our experiments are presented. In *section 2.1*, details about the burner setup and the precursor system are provided. Subsequently, in *section 2.2*, we present some analytical parameters describing the experimental SFS flames utilized. In *section 2.3* it is explained how powder samples were collected and analyzed. The working principle of our TS probe is explained in *section 2.4*. There, the literature in terms of TS probing is reviewed also.

2.1 Operating the SpraySyn burner and utilized precursor compositions

To generate the iron oxide particles, the SpraySyn burner was used which was introduced in 2019 by Schneider et al. as a standard burner to unify SFS studies (Schneider et al. 2019). As shown in **Figure 1**, the burner consists of a nozzle centrally positioned in a porous bronze matrix. The nozzle itself consists of a central capillary (conveying the liquid feed) and a coaxial gap (conveying the dispersion gas). The porous matrix allows two gas streams to flow concentrically through it. Firstly, the pilot flame gas mixture passes the matrix close to the nozzle, necessary for the spray ignition. And secondly, an outer sheath gas flow passes the outer region, aiming for a stabilization of the flame. A major advantage of the SpraySyn burner is the fact, that the internal capillary can be adjusted very precisely via three micrometer screws after burner assembly in order to achieve a rotationally symmetrical flame. Meanwhile, Bieber et al. and Karaminejad et al. found that flames from the SpraySyn burner tend to produce flame pulsations (Karaminejad et al. 2023; Bieber et al. 2021). The time scale of the pulsations is in the lower one-digit millisecond range. Hence, they are not visible to the "naked eye" or even in camera images (typically using higher image exposure times). As shown in their studies, pulsations are a result of an aperiodic ignition of larger liquid feed lumps. Small-sized droplet fractions are shielded physically from the pilot flame to a certain extent as the coaxial dispersion gas piping is oriented parallel to the inner capillary. In contrast, large-sized liquid lumps can pass the dispersion barrier easier due to their higher inertia moment. Subsequently, their ignition lead to the formation of large flame pulsation, representing a more active flame condition.

https://doi.org/10.5194/ar-2023-14
Preprint. Discussion started: 3 November 2023

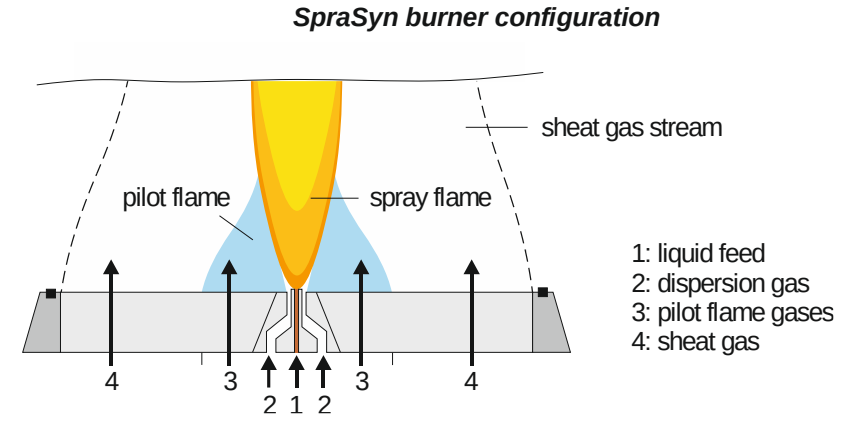

Figure 1: Illustration of the SpraySyn burner working function.

Table 1: Utilized burner operating conditions. Flow rates referred to IUPAC standard temperature and pressure (273.15 K, 101.325 kPa).

dispersion gas	liquid feed	pilot flame gas		sheath gas
O_2	0.1 or 0.2 M INN in EtOH+2-EHA	O_2	CH_4	air
10 L_N min^{-1}	2 mL min^{-1}	2 L_N min^{-1}	16 L_N min^{-1}	120 L_N min^{-1}

The flow rates and gas types used for the burner are shown in **Table 1**. The liquid feed was delivered through the capillary by a syringe pump (KDS Gemini 88 Plus, KD Scientific Inc.) and all gas flows were controlled with mass flow controllers (Bronkhorst High-Tech B.V.). The burner was operated in an open combustion chamber. In our study, two precursor compositions were used, which solely differed in precursor concentration. In particular, either 0.1 M or 0.2 M INN was dissolved in a 35:65 mixture (v/v) of EtOH and 2-EHA. INN was manufactured from Sigma Aldrich (purity >99%), and EtOH was obtained from VWR (MAK free, water content <0.20%-vol). 2-EHA was manufactured from Sigma Aldrich (purity >99%).

At this point, it must be emphasized that the use of 2-EHA is well established in the literature, as its presence suppresses the droplet-to-particle pathway. Hence, if one actually uses INN dissolved in pure alcohols (i.e., without 2-EHA) as precursor composition, large spherical particles >100 nm are generated via the droplet-to-particle synthesis pathway (Tischendorf et al. 2021; Sorvali et al. 2021; Sorvali et al. 2019; Teoh et al. 2010; Strobel und Pratsinis 2011). According to current knowledge, the reason for the benefit of the 2-EHA utilization is the fact, that Fe ions are protected against hydrolysis to non-volatile iron hydroxides. Usually the temperature-driven INN precipitation already takes place at room temperature in some alcohols (Stodt et al. 2019; Keller et al. 2020). As shown by Meierhofer et al, Stodt et al, Angel et al, and Strobel and Pratsinis ester formation and carboxylation take place within the precursor solution in case 2-EHA is present (Meierhofer et al. 2017; Stodt et al. 2019; Angel et al. 2021a; Angel et al. 2020; Angel et al. 2021b; Strobel und Pratsinis 2011), which apparently contributes to the stabilization of the Fe-ions.

https://doi.org/10.5194/ar-2023-14
Preprint. Discussion started: 3 November 2023

AEROSOL Research Discussions

2.2 Relevant analytical parameters

In literature several parameters derived from actual process conditions were identified either influencing the formation of disperse particle properties or impurities. An overview of most important parameter is shown in **Table 2**. There, a brief definition is given for each parameter. Additionally, we listed reference studies which used the corresponding parameter to denote/compare SFS experiments. Most studies intended a parameter variation to examine its impact on the particle formation by in situ diagnostics and/or by characterizing the final powder outcome. At this point it has to be highlighted that all mentioned parameters presented result from analytical calculations considering the burner operation conditions and properties of the precursor solution components. Therefore, by definition, they are independent of the burner type. And as the influence of the burner type and atomization is neglected this way, it is not possible to describe SFS experiments using *only* these parameters.

Table 2: Analytical parameter affecting the particle generation in SFS.

symbol	unit	parameter name	description	references
R_T	-	relative precursor volatility	ratio of the solvent boiling temp. to the melting/decomposition temp. of the precursor	(Jossen et al. 2005)
H	kJ g_{gas}^{-1}	combustion flame enthalpy density	ratio of the flame enthalpy to its gas mass	(Jossen et al. 2005)
Φ	-	oxygen stoichiometry	division of the actual fuel to oxidizer ratio and the stoichiometric fuel to oxidizer ratio	(Strobel und Pratsinis 2009; Carvajal et al. 2020; Sorvali et al. 2021; Sorvali et al. 2019; Li et al. 2013)
f_v	-	particle volume fraction	ratio of the volume occupied by the particle phase to the total flame volume	(Stefanidis et al. 2022)
SLR	-	spray to liquid ratio	ratio of the liquid feed rate to the dispersion gas rate	(Li et al. 2007; Gröhn et al. 2014b; Meierhofer et al. 2020)

As explained in *section 2.1*, two precursor compositions were processed in our study using the SpraySyn burner and we summarized the corresponding parameter set for both synthesis in **Table 3**. As shown there, the influence of changing the INN concentration is rather small. Only f_v is affected considerably. For calculating f_v a conservative gas-phase temperature of 2000 K and a maghemite density of 4.88 g cm^{-3} was assumed. To calculate the reaction balances, we assumed that the streams from pilot flame, dispersion gas, and liquid feed were mix ideally, and species react/oxidize completely (forming Fe_2O_3, H_2O, CO_2, N_2). The utilized reaction equations incl. their enthalpies are shown in the appendix (**Table A 1**). As shown in **Table 3**, the relative precursor volatility should increase *in situ*. This is caused by the fact that EtOH evaporates preferably comparing to 2-EHA from the droplet phase. Hence, the 35:65 mixture (v/v) of EtOH and 2-EHA is present initially, but 2-EHA accumulates *in situ* in the droplet phase due to the EtOH evaporation. A comparison of the vapor pressure functions of 2-EHA, EtOH, and solvent mixture of EtOH and 2-EHA is also shown in the appendix (**Figure A 1**)

https://doi.org/10.5194/ar-2023-14
Preprint. Discussion started: 3 November 2023

INN conc.	0.1 M	0.2 M
solvent	EtOH+2-EHA	EtOH+2-EHA
R_T/-	rises in situ from 1.14 to 1.56	
Φ / -	0.2624	0.2622
H / kJ g^{-1}_{gas}	3.106	3.101
f_v (@2000K)/ -	$1.516x10^{-8}$	$3.029x10^{-8}$
SLR / mL L_N^{-1}	0.2	

Table 3: Comparison of analytical parameters for SFS experiments conducted.

2.3 Powder collection and characterization

Both precursor compositions were utilized for particle generation and corresponding powders were collected by membrane surface filtration. For this purpose, the flame aerosol was extracted above the flame at ~20 cm Height Above Burner (HAB) by a fume hood utilizing a vacuum pump (Mink MM 1144 BV, Dr.-Ing. K. Busch GmbH). The hood was connected with the surface filter by a 1 meter long flexible metal tubing (DN40). The filter medium used was an ePTFE membrane (R+B Filter GmbH). Collected particles can experience thermal induced phase transformations and sintering. Hence, providing a sufficient low temperature close to the membrane is mandatory to obtain a representative powder collective. Concerning iron oxides phase transformations can take place already at temperatures in the lower three digit °C-regime. E.g., some iron hydroxides can transform already 200 °C, and the maghemite-hematite transfer takes place in a range of 400-500 °C (depending on the particle size and purity) (Cornell et al. 2003). Iron oxide phases can also experience sintering. However, sintering usually takes place at even higher temperatures (Rosenberger et al. 2022; German 2014; Mikami et al. 1996). In our experiments, we measured steady-state temperatures in a range 100-150 °C via thermocouple close to the membrane, which represented a sufficient temperature range to avoid phase transformations and sintering. Additionally, a thermal dsintegration of the filtration membrane was excluded at this temperature.

A red-brownish, strongly hydrophobic powder was obtained in both syntheses after one hour of synthesis time. The powders were stored and subsequently characterized by powder analytical methods. To obtain information about the particle phase and the presence of elemental carbon, samples were analyzed by TEM and Raman. Raman spectroscopy was conducted using an inVia™ confocal Raman microscope (Renishaw plc.). A low laser intensity of 1% at 633 nm (0.175 mW) was used to avoid any phase transformations that could occur during Raman measurements otherwise (Hanesch 2009). Each measurement consisted of 50 repetitions, with each repetition lasting 10 seconds, resulting in a total sampling duration of 500 seconds. TEM samples were analyzed using a JEOL JEM-ARM200F high-resolution microscope with Cs-correction and field emission HRTEM-STEM capabilities. Conventional carbon-coated Cu-grids (S160, PLANO GmbH) were used. The TEM grids were dipped into the powders for preparation. Quantitative information about the particle structure properties and the presence of impurities was derived by Brunauer-Emmet-Teller N_2 physisorption (BET), Attenuated-total-reflection-FTIR (ATR-FTIR) and TGA coupled with Differential Scanning Calorimetry and Mass Spectrometry (TGA-DSC-MS). FTIR measurements were conducted on a Vertex® 70 spectroscope. The absorbance was measured in the wavelength range of 370-4500 cm^{-1} with a

https://doi.org/10.5194/ar-2023-14
Preprint. Discussion started: 3 November 2023

resolution of 4 cm^{-1}. A platinum holder was used for ATR measurements. For TGA-DSC-MS, a STA 449 F1 Jupiter® device was employed. The powders were pressed into pellets and heated from 25 to 1000 °C in a silicon carbide oven under either synthetic air or argon as atmosphere (heating rate of 7.5 K min^{-1}). The gas atmosphere during TGA-DSC was monitored by MS using a QMS 403 Aëolos® quadrupole device, and mass to charge (m/z) ratios of 18 (H_2O), 44 (CO_2), and 32 (O_2) were monitored.

By utilizing the BET (Brunauer et al. 1938), the samples mass specific surface area (S_A) was determined using a Quantachrome Autosorb 6 instrument at -196 °C. Prior to the measurements, the samples were vacuum-degassed overnight at 120 °C. The S_A calculation was performed using five points in the relative pressure region between 0.1-0.3. Considering that S_A is given by the ratio of the cumulative surface of all particles, $\sum_i S_i$,, to their cumulative mass, $\sum_i M_i$, an equivalent primary particle diameter $d_{PP,BET}$ can be calculated by equation *(1)*. To define $d_{PP,BET}$, the relation assumes that they are of perfect spherical shape, and uniform size. Hence, $d_{PP,BET}$ can be considered as the samples surface equivalent, mass-weighted average particle diameter. With S_{PP} and V_{PP} as surface and volume of such a primary particle and the equivalent primary particle size, N the total number of primary particles, and ρ the material density:

$$S_A = \frac{\sum_i S_i\,,}{\sum_i M_i} = \frac{\sum_i S_i\,,}{\rho \sum_i V_i} \triangleq \frac{N \cdot S_{PP}}{\rho \cdot N \cdot V_{PP}} = \frac{6}{\rho \cdot d_{PP,BET}} \qquad (1)$$

.

2.4 Thermophoretic sampling and transmission electron microscopy (TS-TEM)

During processing the low-concentrated precursor composition (including 0.1 M INN), particle samples were additionally extracted at two *HAB* positions, namely at 5 cm *HAB* and at 15 cm *HAB*. For this purpose, a customized TS probing system was designed and characterized. At the beginning (*2.4.1*), a short excursion into the literature is made. There, an overview about TS sampler systems developed in the past decades is presented. Note, in this section the focus lies on the design issues for TS probes. Further information in terms of TS theory (e.g., concerning determination of in-situ particle volume fractions and particle fractal dimensions by quantitative image post processing), the reader is referred to the literature listed there. In the subsequent section, the principle of our TS system is explained (*2.4.2*). In the last section, it is explained to what extent the TEM-grids exposure time can be adjusted by using our sampler technique (*2.4.3*).

2.4.1 TS theoretical background

TS-TEM has been widely used in the past to study soot, primarily in diffusion flames, and established as essential technique for obtaining direct information about particle morphology through TEM analysis. TS-TEM offers several advantages over other experimental methods, particularly in terms of providing direct insights into particle crystallinity and shape. This enables the identification of carbon depositions, representing amorphous particle coatings and amorphous aggregates. Although TS-TEM has become a standard procedure, different TS probes have been developed over the last years, which differ in their

https://doi.org/10.5194/ar-2023-14
Preprint. Discussion started: 3 November 2023

specifications and their working principles. The initial TS method was introduced by Dobbins and Megaridis, where a TEM sample grid was inserted into a diffusion flame using a pneumatic cylinder (Dobbins und C. M. Megaridis 1987). While many researchers have replicated this approach, more complex and versatile probes have been developed. For instance, Leschowski et al. designed samplers with sufficient chamber sealings for particle extraction in high-pressure chambers (Leschowski et al. 2014). Varges et al. developed a highly automated sampler capable of continuous extraction of multiple samples over time using a multi-probe system (Vargas und Gülder 2016). A summary of studies utilizing TS probes which can be used for TEM evaluation is provided in **Table 4**. The studies are compared in respect to their sampling time (t_s) as well as the gas phase process and material systems they were applied to. Probes that deviate significantly from the approach of Dobbins and Megaridis are highlighted, and their methodological differences are briefly explained. Based on this brief review of the literature, three general considerations for probe design emerged in our study. First, TS can perturb the reactive flow, potentially leading to experimental biases (Lee et al. 2008a). To minimize this effect, TS-probes (which are typically flat in at least one dimension) should be oriented parallel to the flow field. Second, the ability to adjust t_s is advantageous for various reasons. It is particularly beneficial to adjust lower t_s to prevent grid thermal decomposition and achieve low grid loading densities. This is especially mandatory if the identification of individual particle structures is aimed. Third, way sampling which means that particles are sampled during the grid's traversal to the sample position, can lead to a bias in the extracted particle ensemble, and has to be considered. Two approaches exist to deal with this last issue. One option is to adapt very high sampling times compared to the traversing time, making the bias simply negligible. Alternatively, the TEM sample grid can be physically protected/shielded from the hot flame atmosphere during passage. In case the latter approach is used, technically advanced probing systems are necessary, which can be referred to as *shutter techniques* due to their principle. Usually, those techniques also allow a flexible adjustment of t_s, and hence, they represent the state of the art in TS-probe types. In summary, TS probe designs have addressed issues related to flow perturbation, adjustable sampling times, and way sampling bias. Those issues were considered in our probe design, and we also tailored a shutter TS probe, allowing a flexible adjustment of the grid exposure time, t_s.

Table 4: Comparison of experimental reports which utilized TS-TEM. The literature was compared with respect to the material system, the process type, the sampling time, but also to the technical TS probe specifications as far as explained by the authors. Most reports utilized a comparable TS probe to the initial approach of Dobbins & Megaridis (Dobbins und C. M. Megaridis 1987). In case major adaptions/new concepts were applied and developed, reports are highlighted (blue-coloured rows). Some probes protect the TEM sample grid during its translation to the sample position and can be referred to as shutter techniques. Although we comprehensively compared a variety of literature references, we assume an unknown amount of possible other principles that exist in various laboratories. Some of them might have not been published so far. Abbreviations: DF = Diffusion Flame, L-CVP = Laser Chemical Vapor Precipitation, SFS = Spray Flame Synthesis, NI = No Information Found.

source	material	process	specifications of the TS probe used	sampling time, t_s	shutter technique?
(Dobbins und C. M. Megaridis 1987)	Soot	DF	First publication: TS by using a dual acting pneumatic cylinder. Sampling- and injection durations were recorded.	30 - 120 ms	no
(Hurd und Flowder 1988)	SiO_2	DF	(Dobbins und C. M. Megaridis 1987)	500 ms	no

https://doi.org/10.5194/ar-2023-14
Preprint. Discussion started: 3 November 2023

(Megaridis und Dobbins 1990)	Soot	DF	(Dobbins und C. M. Megaridis 1987)	36 ms	no
(Hung und Katz 1992)	TiO_2-SiO_2 composite	DF	(Dobbins und C. M. Megaridis 1987)	NI	no
(Koylu und Faeth 1992)	Soot	DF	(Dobbins und C. M. Megaridis 1987)	several seconds	no
(J. Cai/N. Lu/C. M. Sorensen 1993)	Soot	DF	(Dobbins und C. M. Megaridis 1987)	15 ms	no
(Koylu et al. 1995)	Soot, Al_2O_3	DF	(Dobbins und C. M. Megaridis 1987)	NI	no
(Ma et al. 1995)	Soot	DF	Utilization of a spring-loaded system instead of a pneumatic cylinder.	28-128 ms	no
(Sorensen und Feke 1996)	Soot	DF	(Dobbins und C. M. Megaridis 1987)	15 ms	no
(Xing et al. 1996)	Al_2O_3	DF	(Dobbins und C. M. Megaridis 1987)	70 ms	no
(Koylu et al. 1997)	Soot	DF	(Dobbins und C. M. Megaridis 1987)	NI	no
(Kruis et al. 1998)	Si_3N_4	L-CVP	Automated sample grid exposure under defined atmosphere directly after the extraction	NI	no
(Zhang und Megaridis 1998)	Soot	DF	(Dobbins und C. M. Megaridis 1987)	30 ms	no
(Cho 1999)	SiO_2	DF	Protecting the grid during its transfer to the sampling position by a flat protector shield. A second pneumatic cylinder is utilized to reject the shield for the grid exposure.	50 ms	yes
(Choi et al. 1999)	SiO_2	DF	(Cho 1999)	50 ms	yes
(Heidermann et al. 1999)	Soot	DF	(Dobbins und C. M. Megaridis 1987)	<100 ms	no
(Xing, Y., Koylu, U. Y. und Rosner 1999)	Al_2O_3	DF	(Dobbins und C. M. Megaridis 1987)	40-100 ms	no
(Cho und Choi 2000)	SiO_2	DF	(Cho 1999)	50 ms	yes
(Lee und Choi 2000)	SiO_2	DF	(Cho 1999)	70 ms	yes
(Arabi-Katbi et al. 2001)	TiO_2	DF	(Dobbins und C. M. Megaridis 1987)	50 ms	no
(Janzen et al. 2002)	Fe_2O_3, ZnO, GeO_2	Plasma, DF	(Dobbins und C. M. Megaridis 1987)	NI	no
(Kammler 2002)	TiO_2	DF	(Dobbins und C. M. Megaridis 1987)	50 ms	no
(Tsantilis et al. 2002)	TiO_2	DF	(Dobbins und C. M. Megaridis 1987)	NI	no
(Hu et al. 2003)	Soot	DF	Protecting the grid during its transfer to the sampling position by a protective tube. The grid exits the tube after reaching the sample position.	60-110 ms	yes
(Kammler et al. 2003)	TiO_2	DF	(Dobbins und C. M. Megaridis 1987)	50 ms	no
(Hu und Koylu 2004)	Soot	DF	(Dobbins und C. M. Megaridis 1987)	15-40 ms	no
(Mueller et al. 2004)	ZrO_2	SFS	(Dobbins und C. M. Megaridis 1987)	50 ms	no
(D'Alessio et al. 2005)	Soot	DF	(Dobbins und C. M. Megaridis 1987)	20 ms	no
(Kammler et al. 2005)	SiO_2	DF	(Dobbins und C. M. Megaridis 1987)	NI	no
(Neer und Koylu 2006)	Soot	Diesel Engine	(Dobbins und C. M. Megaridis 1987)	100-700 ms	no
(Ifeacho et al. 2007)	SnO_2	DF	NI	NI	NI
(Lapuerta et al. 2007)	Soot	Diesel Engine	(Dobbins und C. M. Megaridis 1987)	600 ms	no
(Lee et al. 2008a)	SiO_2	DF	Protecting the grid during its transfer to the sampling position by a flat protector shield. A second pneumatic cylinder is utilized to reject the shield for sample grid exposure. Multiple sample holder dimensions available.	50 ms	yes
(Reimann et al. 2009)	Soot	DF	NI	NI	NI
(Oltmann et al. 2010)	Soot	DF	Utilization of a spring-loaded system instead of a pneumatic cylinder.	100 ms	NI
(Oltmann et al. 2012)	Soot	DF	NI	30-100 ms	NI
(Gröhn et al. 2014a)	ZrO_2	SFS	(Dobbins und C. M. Megaridis 1987)	10-150 ms	no
(Leschowski et al. 2014)	Soot	DF	Utilization of pressure resistant components to allow sample extraction from high-pressure	67 ms -1873 ms	no

https://doi.org/10.5194/ar-2023-14
Preprint. Discussion started: 3 November 2023

			reactors. Mountable by flange-sealing at reactor wall/window.		
(Leschowski et al. 2015)	Soot	DF	(Leschowski et al. 2014)	100 ms	no
(Altenhoff et al. 2016)	Soot	DF	Utilization of an electrical actor instead of a pneumatic cylinder allowing the adaption of more precise sampling times.	3-100 ms	no
(Goudeli et al. 2016)	ZrO_2	SFS	(Dobbins und C. M. Megaridis 1987)	40-110 ms	no
(Vargas und Gülder 2016)	Soot	DF	Fully automated device to extract samples subsequent on multiple grids. The grids are mounted on a rotational plate-system which is driven by a stepwise acting rotor. The sampler has to be implemented within the reactor space.	3-8 ms	no
(Vargas und Gülder 2017)	Soot	DF	(Vargas und Gülder 2016)	3-8 ms	no
(Carbone et al. 2017)	Soot	DF	New approach without using conventional TEM sampling grids. Instead, a SiC wire (13.5 µm thickness) is traversed through to process volume leading to thermophoretic deposition. TEM analysis of particles attached on the wire.	28-110 ms	no
(Kunze et al. 2019)	SiO_2	Plasma	Protecting the grid during its transfer to the sampling position by a hollow rectangular protector shield. The grid exits the tube after reaching the sample due to its inertia motion. The necessary back force is provided by a spring-system.	5-10 ms	yes
(Suleiman et al. 2021)	FeO	DF and SFS	(Kunze et al. 2019)	14 ms	yes
This work	Fe2O3	SFS	The TEM-grid is located at a slider which is protected by a stainless-steel protector. The protector has a small recess. For sampling, the slider movement is initiated (forced back by a spring). Hence, the grid passes the recess and is temporarily exposed to the environment.	1-30 ms	yes

.4.2 Sampling probe working principle and sample preparation

Figure 2-(a) illustrates the key steps of the sampling procedure, captured by high-speed monitoring without the presence of a flame. For this purpose, a Fastcam SA-X2 1080K-M3 camera was employed (software: Photron Fastcam Viewer 4 from the manufacturer Photron Deutschland GmbH, Reitlingen, Germany). The camera settings were configured to achieve a temporal resolution of 12 500 frames per second with a resolution of 1024x1024 pixels. As shown in panel 1, the probe is initially positioned at the desired sampling location using a pneumatic cylinder, which takes approximately 100 ms. During this time the TEM-grid (which is attached on a slim metal slider) is protected by a stainless-steel protector. Note, in panel 1, the position of the inner slider incl. the TEM-grid is indicated. Once the sampling position is reached (panel 2), sampling is automatically activated by a proximity sensor. Then, the TEM grid (which is mounted on an inner slider), is pulled back passing a recess within the protector. As the hot flame aerosol streams through the recess, thermophoretic particle deposition takes place in this time span (panel 3). Subsequent to the particle extraction, the TEM-grid is shielded again from the surrounding environment (panel 4). Note, the protector parts on both sides of the recess need to be physically connected, and as visualized, a bridge structure positioned downstream of the sampling position was used for this purpose. High-speed observations showed that the flame aerosol flows unimpeded through the sample recess and was not affected significantly by the presence of the bridge

https://doi.org/10.5194/ar-2023-14
Preprint. Discussion started: 3 November 2023

construction. To provide a sense of scale between the TS-sampler and the flame, **Figure 2-(b)** presents a photograph of the experimental spray flame using the SpraySyn burner (taken by SLR camera).

To explain the sampling principle more in detail a full illustration of the TS probe is presented in **Figure 2-(b)**. Note, this illustration shows the prepared TS-probe (ready to use), and hence, the TEM-grid is positioned at the right side of the recess. For better visualization the front side of the protector is illustrated transparent (light blue). As shown, the overall TS probe can be divided into three main parts: the shutter head (as already seen in **Figure 2-a**) a quick mounting connector, and the pneumatic cylinder periphery. The development of the quick mounting connector was useful to allow a fast and easy mounting/reassembly of the shutter head from the pneumatic cylinder periphery. As shown, the left side of the slider is attached to a tensioned spring, providing the driving force for the slider movement. To hold the slider in position, a solenoid-controlled pin is used (the pin passes a drilling in the slider). When the probe is inserted into the process for sampling, a proximity sensor gives an electric signal to the solenoid which consequently goes ahead with the pin rejection. Note, as the shutter head can be demounted easily, the probe preparation can be conducted within a clean air working bench. The preparation includes several easy steps: Firstly, a TEM sample grid is attached to the tip of a slider using adhesive copper tape. Subsequently, the slider including the grid is mounted inside the stainless steel protector, as depicted in **Figure 2-(c)**. In this position, the slider is connected to the spring. Next, the spring is tensioned by shifting the position of the spring tensioner. As mentioned, the slider is hold back in position due to the solenoid-controlled pin. As the spring tensioner can be positioned along a certain length, a variety of different spring geometries can be used in our TS probe.

https://doi.org/10.5194/ar-2023-14
Preprint. Discussion started: 3 November 2023

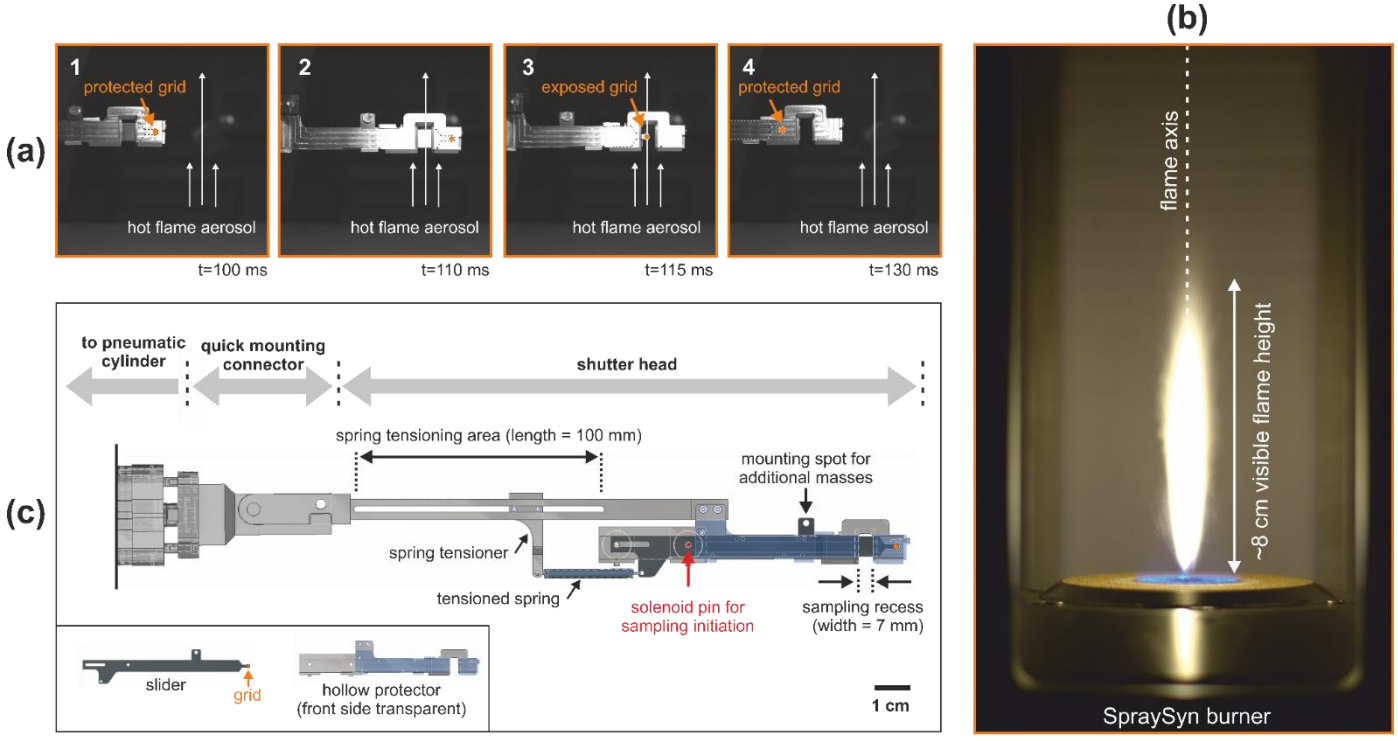

Figure 2: Visualization of the sampling principle and the dimension of our TS shutter probe. **(a)**: visualization of the sampling process as monitored by high-speed monitoring. Note, the grid is mounted on a flat slider which is located within a hollow steel protector. Hence, the slider geometry is indicated by dotted lines. Panel explanation to **(a)**: **1**: Photo taken during traversing the probe by means of a pneumatic cylinder in direction to the sample position. The grid is attached on a slider and is shielded against the environment by the hollow steel protector. **2**: Reaching the sample position. Sampling is activated automatically by means of a proximity sensor. **3**: The slider is forced back by a spring. Hence, the TEM-grid passes the recess and thermophoretic particle deposition takes place in this moment. **4**: Automated rejection takes place. **(b)**: photography of the experimental spray flame taken via single-lens reflex (SLR) camera. **(c)**: schematic construction of the TS probe. Note different scales.

2.4.3 Adjustment of the grid exposure time, t_s

The sampling time, t_s, represents the time the grid needs to cross the exposed area of the sampling recess. As the movement of the slider is initiated by a spring, it can be described as a harmonic oscillation, visualized in **Figure 3**. There, the grid position is illustrated simplified by a point (representing the grid centre). In fact, the grid has a diameter of 3.05 mm. As visualized, the grid enters the sampling recess at position x_{en} and exits at position x_{ex}, corresponding to times t_{en} and t_{ex}. By considering the grids movement as a harmonic oscillation, t_s can be calculated using equation *(2)*. There, k represents the spring constant, x_i is the initial spring extension, and m_{sl} is the mass of the slider.

$$t_S = t_{ex} - t_{en} = \frac{\cos^{-1}\left(\frac{x_{ex}}{x_i}\right) - \cos^{-1}\left(\frac{x_{en}}{x_i}\right)}{\sqrt{k/m_{sl}}} \qquad (2)$$

https://doi.org/10.5194/ar-2023-14
Preprint. Discussion started: 3 November 2023

The samplers' geometrical parameters are fixed. In particular, the initial distance of the grid centre to the sample recess is 10 mm, and the recess width is 7 mm. Hence, the grid enters the recess at 10 mm and exits at 17 mm. Although those geometrical parameters are fixed, the sampling time t_s can be adjusted by changing k, m_{sl}, and x_i. The initial spring extension x_i can be easily modified by adjusting the position of the spring tensioner. In our laboratory, we kept the slider thickness constant, and slider mass was changed by adding additional mass to the slider. Therefore, our sliders have a 3 mm drilling hole on their top. The drilling hole is highlighted in **Figure 2-(b)**. The spring constant k can be modified by using different types of springs. In our approach, we used springs from Gutekunst Co. KG as listed in **Table 5**, which are suitable for our probe for geometrical reasons . In this brief overview, we show the possible ranges of t_s for each spring type, showing a theoretical range from approximately 0.5 ms up to 30 ms. For each spring type, the lower t_s boundary was calculated using m_{sl} = 2.18 g (the minimal slider mass without additional masses) and x_i = 80 mm as the maximum initial spring extension. The upper thresholds were calculated using m_{sl} = 20 g (which was the maximum total slider mass we used), and x_i = 28 mm as the minimum spring extension. Note, that the *theoretical* minimum spring extension is 27 mm because the grid travels an additional 10 mm after exiting the recess until it reaches a stopper at x_{end}. Thus, the minimal theoretical x_i is equal to 10+7+10=27 mm, and not 28 mm. However, we recommend using 28 mm instead of 27 mm for the minimal x_i value to ensure that the slider is still forced slightly after reaching the end position, x_{end}.

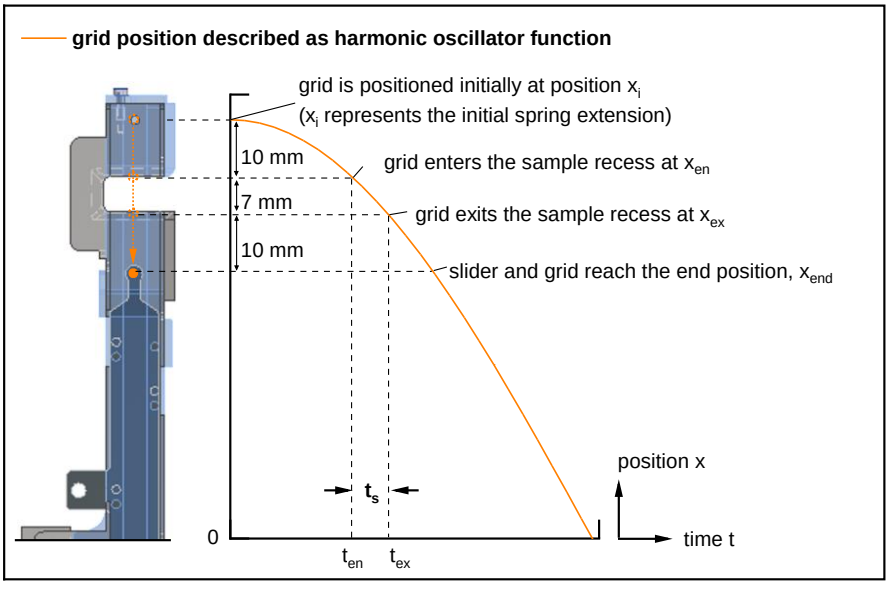

Figure 3: Illustration of the grid movement as part of a harmonic oscillation function, according to equation (2). The parameter **x** represents the position of the grid centre. The sampling interval $\mathbf{t_s}$ is determined by $\mathbf{t_{en}}$ and $\mathbf{t_{ex}}$.

https://doi.org/10.5194/ar-2023-14
Preprint. Discussion started: 3 November 2023

AEROSOL Research Discussions

spring type	k / N mm-1	t_s / ms
RZ-006KI	0.002	3.0 – 28.7
RZ-006JI	0.004	2.1 – 20.3
RZ-003AI	0.009	1.4 – 13.5
RZ-015KI	0.017	1.0 – 9.9
Z-039I	0.064	0.5 – 5.1
Z-051KI	0.097	0.4 – 4.1

Table 5: Recommended spring types including their constants *k*, which can be utilized for our TS probe including their theoretical range of sampling time t_s by changing the slider mass m_s and initial spring extension x_i.

In our approach particles were extracted from the SFS process using Z-039I (k=0.064 N/mm) as spring type, and the adjustment of t_s was validated through high-speed monitoring, a priori. **Figure 4** compares experimental and theoretical sampling times. As shown, the Z-039I spring allows for arbitrary changes in t_s in the range of approximately 1-5 ms by adjusting either the initial spring extension, x_i **(a)**, or the slider mass, m_{sl} **(b)**.

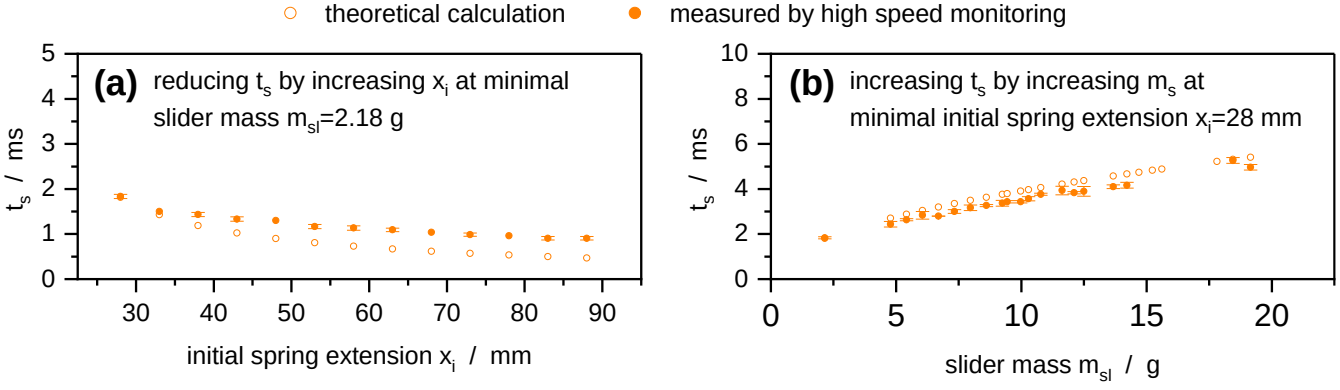

Figure 4: Comparison of theoretical and experimental sampling times (derived by high speed imaging utilizing a spring type Z-039I (**k**=0.064)).

In **(a)** x_i was increased stepwise at minimal slider mass (m_{sl}=2.18 g). This way t_s decreased from approximately 2 to 1 ms. In **(b)** the slider mass was increased at fixed, minimal x_i=28 mm. This way t_s increased from approximately 2-5 ms. It is important to note that the data presented is exemplary, as arbitrary other combinations of m_{sl} and x_i are possible. For the experimental parameter set considered here, t_s was determined three times via high speed monitoring, and the results were highly reproducible. Note, there are error bars in **Figure 4**. However, they are mostly barely visible, especially in **(a)**. Interestingly, the experimental values systematically differed from the theoretical ones: For minimal mass (**a**) the experimental values of the sampling time were significantly longer than calculated. In case of minimal initial spring extension (**b**) however, the experimental values of the sampling time are rather slightly shorter than theoretically expected. We attribute the difference between experimental and theoretical values to two reasons. First, the tendency observed in **(a)** suggests that an increase in x_i leads to increased friction between the slider and the protector. This can be explained by the asymmetrical forces exerted by the spring on the inner slider due to the construction. As a result, the upper edge of the slider is slightly pushed against the inner wall of the protector. Second, the tendencies observed in **(b)** indicate that the real spring constants slightly differ from

https://doi.org/10.5194/ar-2023-14
Preprint. Discussion started: 3 November 2023

the theoretical ones, as an underestimation of k in equation *(1)* leads to systematically higher sampling times. This systematic overestimation of t_s counteracts the influence of friction and becomes more relevant at low initial spring extensions or high sampling times (as shown in panel **b**). We want to mention that there may be further minor effects contributing to the discrepancy between theoretical and practical t_s values. Examples are the neglection of the acceleration of the spring mass itself, neglecting the effects of vibrations within the spring, and neglecting gas friction within the protector.

https://doi.org/10.5194/ar-2023-14
Preprint. Discussion started: 3 November 2023

3 Results and discussion

3.1 Powder characterization

Particles were generated by the SpraySyn burner using two precursor compositions (either 0.1 M or 0.2 M INN dissolved in EtOH+2-EHA as solvent) and collected by surface filtration. Subsequently they have been characterized by powder analytics. This way information concerning the particle phase, sizes, and purity were derived.

3.1.1 Evaluation of the particle phase and proof for carbon content

To detect carbon contaminations, Raman and TEM are established techniques in the literature. In this regard TEM is the more *direct* method, because the morphology of the particle samples is directly visible. As shown for example by Li et al., Carvajal et al., and Herrmann et al. carbon can be easily distinguished from iron oxides (which are usually in crystalline form) due to its amorphous structure (Li et al. 2013; Carvajal et al. 2020; Herrmann et al. 2009). Raman was used by Strobel and Pratsinis for carbon identification. In terms of Raman, the authors examined if the characteristic soot bands emerge in the powder Raman spectra. Those bands are the so-called G and D bands and are present at 1300 and 1590 cm^{-1}, respectively (Strobel und Pratsinis 2009). **Figure 5-(a)** shows several typical TEM images for the powder derived from processing the low concentrated precursor solution (0.1 M INN). In **(b)** the powders corresponding Raman spectrum is given.

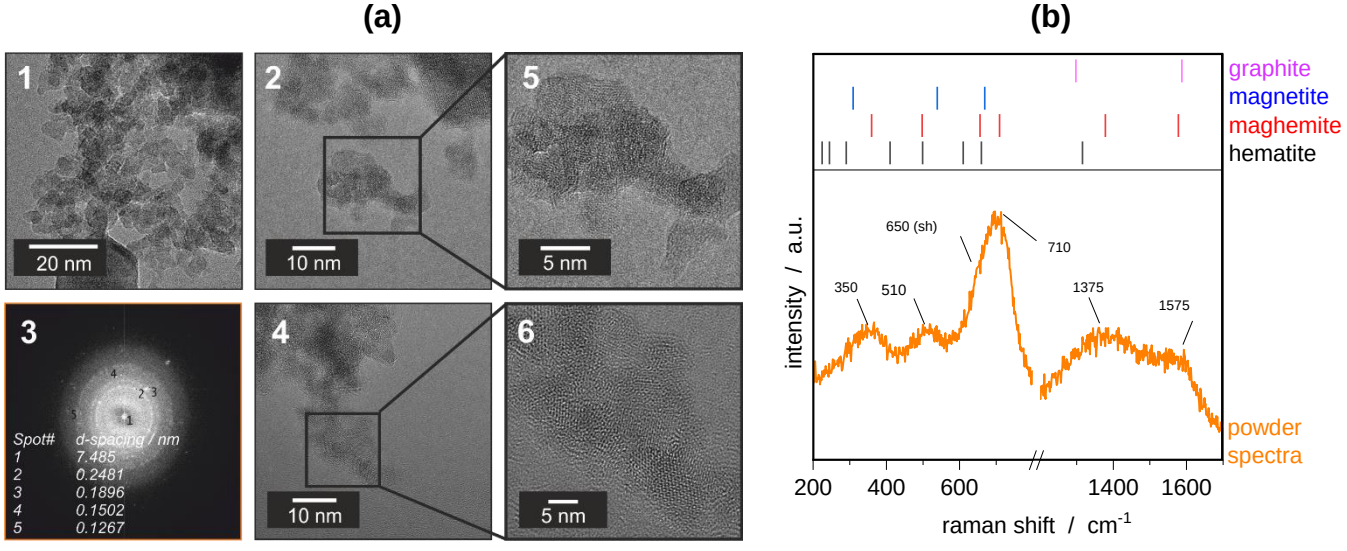

Figure 5: Proof for carbon by TEM **(a)** and Raman spectroscopy **(b)** for iron oxide samples made by SpraySyn and using 0.1 M INN dissolved in EtOH and 2-EHA as precursor composition. Particles were collected by surface filtration. References explained in the text.

As illustrated in **(a)**, the grid was covered by particles which were arranged close to each other. Mostly spherical primary particles were observed, roughly with sizes <10 nm from first point of view (panel 1). As particles were closely arranged, it was not possible to identify individual aggregate/agglomerate structures. It is noteworthy, that a minor fraction of hexagonal particles with sizes >20 nm was also present, presumably originating from a suppressed droplet pathway. By TEM, the product

https://doi.org/10.5194/ar-2023-14
Preprint. Discussion started: 3 November 2023

particles crystallinity was proven for several particle ensembles using Fast Fourier Transformation (FFT). As shown in panel 3 the corresponding diffraction pattern indicated the presence of maghemite. By TEM, no evidence of amorphous particles and/or amorphous particle coatings was found which would have indicated the presence of soot as contamination. Admittedly, some very small particles appeared to be amorphous at first glance (exemplary shown in panel 2 and 4). However, under high magnification (panel 5, 6), crystal planes could be easily detected even for those small particles, indicating crystalline iron oxides. FFT reflections which were exemplarily derived at several positions were in agreement with the Raman measurements, since they also indicated a maghemite presence. At this point, it must be briefly emphasized that Raman represents a simple method to detect iron oxides based on their differences in spectrum <1000 cm^{-1}. The Raman spectrum in **(b)** is therefore compared with references for maghemite, magnetite, and hematite from de Faria et al. (Faria et al. 1997). Note, we compared the experimental features to a larger amount of literature data (see **Table A 2** in the appendix). The comparison illustrates that references from de Faria et al. can be considered as representative. According to the literature, hematite shows seven active phonons namely at ~225-230 (A_{1g}), ~245-250 (E_g), ~290-295 (E_g), ~299-302 (E_g), ~407-414 (E_g), ~491-500 (A_{1g}), and 608-615 (E_g) cm^{-1}. The vibration at ~290-295 cm^{-1} is the most intense, followed by that at ~225-230 cm^{-1}. In addition, a longitudinal vibration at about 654-663 cm^{-1} may also become active if impurities and crystal defects are present. The peaks of hematite are usually very sharp. In contrast to hematite, three main characteristic vibrations have been described in the literature for maghemite, which usually form quite broad maxima. They exist at ~350-381 (T_{2g}), 486-512 (E_g), and 700-730 (A_{1g}) cm^{-1}. Some authors (such as de Faria et al.) have also described that a shoulder can form at 665-670 cm^{-1}. Due to the structural similarity, magnetite also forms three broad phonons, namely at ~300-310, ~332-554, and ~661-672 cm^{-1}. As seen in **(b)**, the experimental positions of the peaks were positioned at 350, 510, and 710 cm^{-1}. Also, a weak shoulder existed at about 650 cm^{-1}. Therefore, the positions of the peaks clearly indicate maghemite as the main phase. Interestingly in the higher wavenumber-regions the Raman spectra showed the presence of two broad maxima, close to the position of the graphite D- and G- bands. However, no graphite traces were detected in the powder by TEM. Hence, without examining the samples by TEM, the presence of these bands could falsely suggest a graphite presence, but in this case, they are likely to belong to the maghemite spectrum. As shown by de Faria et al., the maghemite phase can also give rise to two vibrations in higher wavenumber regions (see referred maxima positions for maghemite in **(b)**).

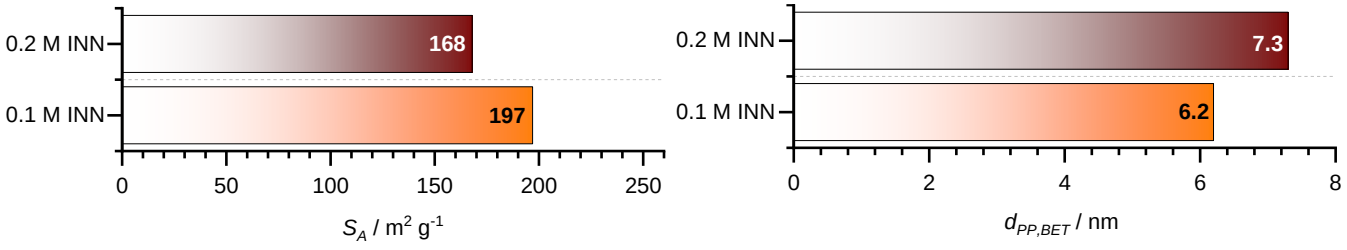

Figure 6: BET data for maghemite samples prepared by SpraySyn and utilizing two concentrations of INN as precursor dissolved in EtOH and 2-EHA. Particles were collected by surface filtration.

https://doi.org/10.5194/ar-2023-14
Preprint. Discussion started: 3 November 2023

As can be seen from the TEM illustrations (in particular from panel 1), primary particle sizes were roughly <10 nm. To obtain further information about the average primary particle diameter, equation (1) was used. Hence, the primary particles equivalence diameter $d_{PP,BET}$ was derived by considering the BET specific surface area (S_A). From the comparison of the BET values (**Figure 6**) it can be seen, that a smaller specific surface area, was derived by processing a higher precursor concentration. Which indicates a larger equivalence diameter in consequence. For the calculation of $d_{PP,BET}$ the density of maghemite of 4.88 g cm^{-3} was used.

3.1.2 Identification of surface-bond carbonates and carboxylates

Even if powder samples appear to be pure by TEM microscopy, small amounts of impurities still may be present. Their existence can be verified by complementary techniques such as ATR-FTIR and TGA-DSC-MS. In this regard, IR measurements offer the possibility to make qualitative statements about existing bond types and hence indicate the presence of functional groups on the particle surface according to the IR-active vibrations in the powder spectrum. The ratios of the peak intensities also allow semi-quantitative statements. The ATR-FTIR spectra of both powders are compared in **Figure 7**.

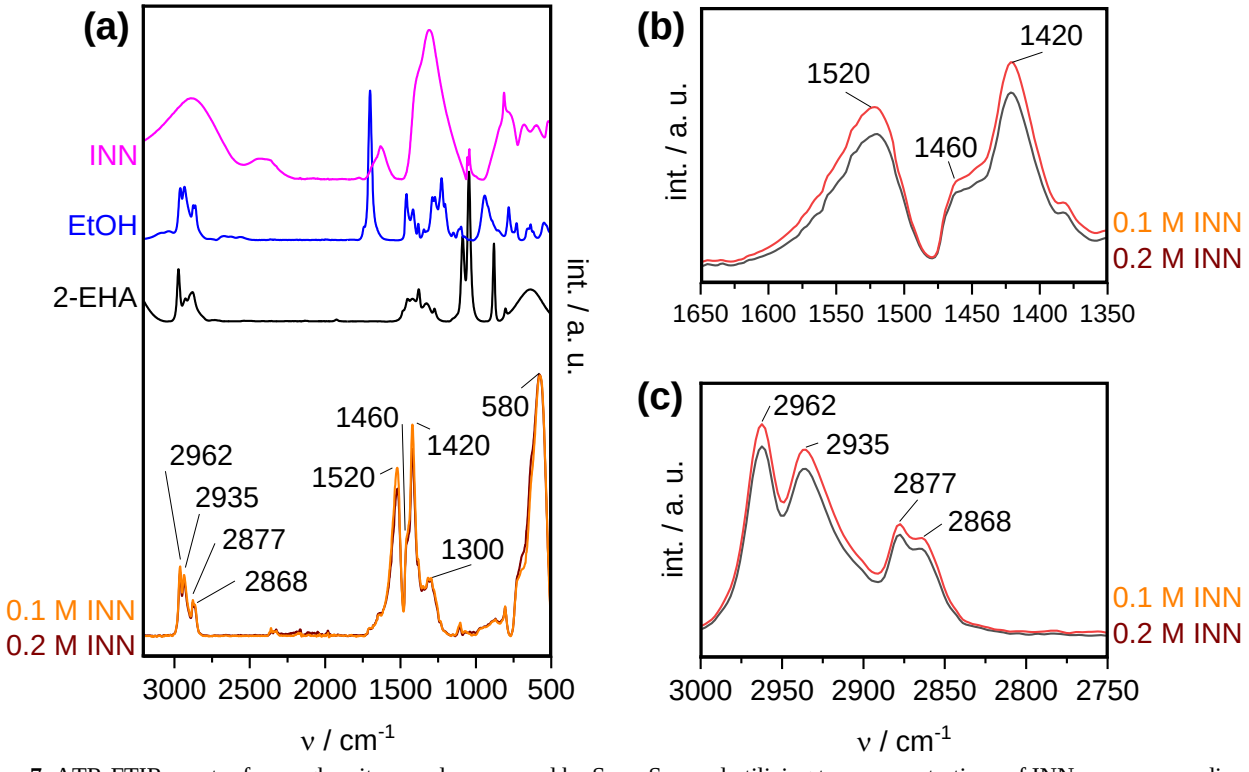

Figure 7: ATR-FTIR spectra for maghemite samples prepared by SpraySyn and utilizing two concentrations of INN as precursor dissolved in EtOH and 2-EHA. Particles were collected by surface filtration. **(a)**: comparison of sample spectra to spectra of the precursor formulation components (INN, EtOH, 2-EHA), **(b)**: spectra magnification in 1650-1350 cm^{-1}, **(c)**: spectra magnification in 3000-2750 cm^{-1}.

https://doi.org/10.5194/ar-2023-14
Preprint. Discussion started: 3 November 2023

In all sub-panels, the powder spectra were normalized to their local maximum at ~600 cm^{-1} representing the product-phase vibration (FeO vibrations). As indicated in **(a)** a single local maximum was found at the 580 cm^{-1} location for both samples. The presence of a single maxima at this position is characteristic of small-scaled vacancy disordered maghemite. This was demonstrated, for example, by Li et al. on SFS-produced maghemite with XRD-crystallite sizes <8 nm (Li et al. 2007). Hence, in terms of phase identification, the FTIR spectra are therefore in agreement with the Raman and TEM conclusions. As also shown in **(a)**, both samples showed further intensely pronounced peaks in the higher wavelength range, unambiguously revealing the presence of organic species. Since we did not excluded a priori that feed components (INN, EtOH and 2-EHA) could enter the surface filter (e.g., in case non-burned droplets bypass the flame), we determined the spectra of these pure substances. As shown in **(a)**, the powder spectra differed clearly from each component's spectrum, so the presence of droplet residues could be ruled out. To identify the impurities, the dominant peak positions/shapes were subsequently compared to literature data. As can be seen, maxima were positioned at 2962, 2935, 2877, 2867, 1645, 1520, 1420, and 1300 cm^{-1}. In addition, a slight shoulder existed at 1460 cm^{-1}. The quartet of vibrations at 2962, 2935, 2877, and 2867 cm^{-1} was found to be due to stretch vibrations of methyl and methylene groups (CH_2, CH_3), indicating the presence of aliphatic structures (Zhu und Hill R. H. 2002; Lee et al. 2008b). Moreover, according to the literature, the strongly pronounced double peak at 1420 and 1520 cm^{-1} indicates the presence of surface-bound carboxylates ($R\text{-}COO^-$) and/or carbonates (CO_3^{2-}). Note, the double peak evolves from their C-O stretch vibrations. Possibly, the aliphatic groups are therefore associated in the molecular rest (R) of carboxylates. At this point, it must be emphasized that free carboxylates and carbonates show the stretch of their C-O groups at *one* wavelength (Bargar et al. 2005). However, as soon as the oxygen atoms are bound other species, a split of the C-O vibrations into *two* vibrational levels takes place, namely a symmetric and an asymmetric stretch (Bargar et al. 2005). Typically, carboxylates and carbonates form complex bonds with metal atoms close to the particle surface, and a variety of different bond coordination exist (monodendate, bidendate, etc.). The exact position of the resulting double peaks depends on both the bond type and the bonding ligand's chemical structure. Due to this sensitivity, various FTIR references have been published for a wide range of possible carbonate/carboxylate compounds with iron oxides. For example, Do et al. observed vibrations split into 1518 and 1438 cm^{-1} for oleic acid-coated iron oxides (Huu Do et al. 2013), and Lee et al. reported oleic acid carboxylation vibrations on maghemite surfaces at 1550 and 1433 cm^{-1} (Lee et al. 2008b). Regarding carbonates, Rémazeilles measured spectra of synthesized chukanovide, $Fe_2(OH)_2CO_3$, showing different carbonate vibrations at 1525, 1465, 1401, and 1357 cm^{-1} (Rémazeilles und Refait 2009). In terms of the SFS it was already stated in literature that components from the gas phase can bind on particle surfaces (Grimm et al. 1997a; Grimm et al. 1997b; Alkan et al. 2020). Consequently, it should be assumed that small particles or powders with high specific surface area can carry a higher relative number of impurities. And in fact, the powder sample derived from 0.1 M INN (which had the higher S_A-value) showed a higher relative intensity of all organic vibrations (relative to Fe-O vibration). To visualize this phenomenon, magnifications are provided in **Figure 7-(b)** and **(c)**.

Subsequently to the ATR-FTIR spectroscopy, TGA-DSC-MS measurements were performed for two reasons. First, we wanted to use the measurement to quantitatively determine the relative mass fraction of impurities in both powders. And second, we

https://doi.org/10.5194/ar-2023-14
Preprint. Discussion started: 3 November 2023

wanted to check how the organic impurities behave at higher temperatures. The latter aspect was addressed to answer the question if the manufactured powders could be purified by thermal treatment (e.g., in a laboratory furnace). The two powders were heated up to 1000 °C in the TGA-DSC, and the gas atmosphere was monitored online by MS. In latter regard, m/z ratios of 18 (H_2O), 32 (O_2), and 44 (CO_2) were traced. For each powder type, one sample fraction was exposed in synthetic air, another one in argon. **Figure 8** shows the complete TGA-DSC-MS data for the sample from 0.1 M INN. Qualitatively, the sample from 0.2 M showed the identical thermal behavior. The quantitative differences between the two samples will be discussed in the next subsection.

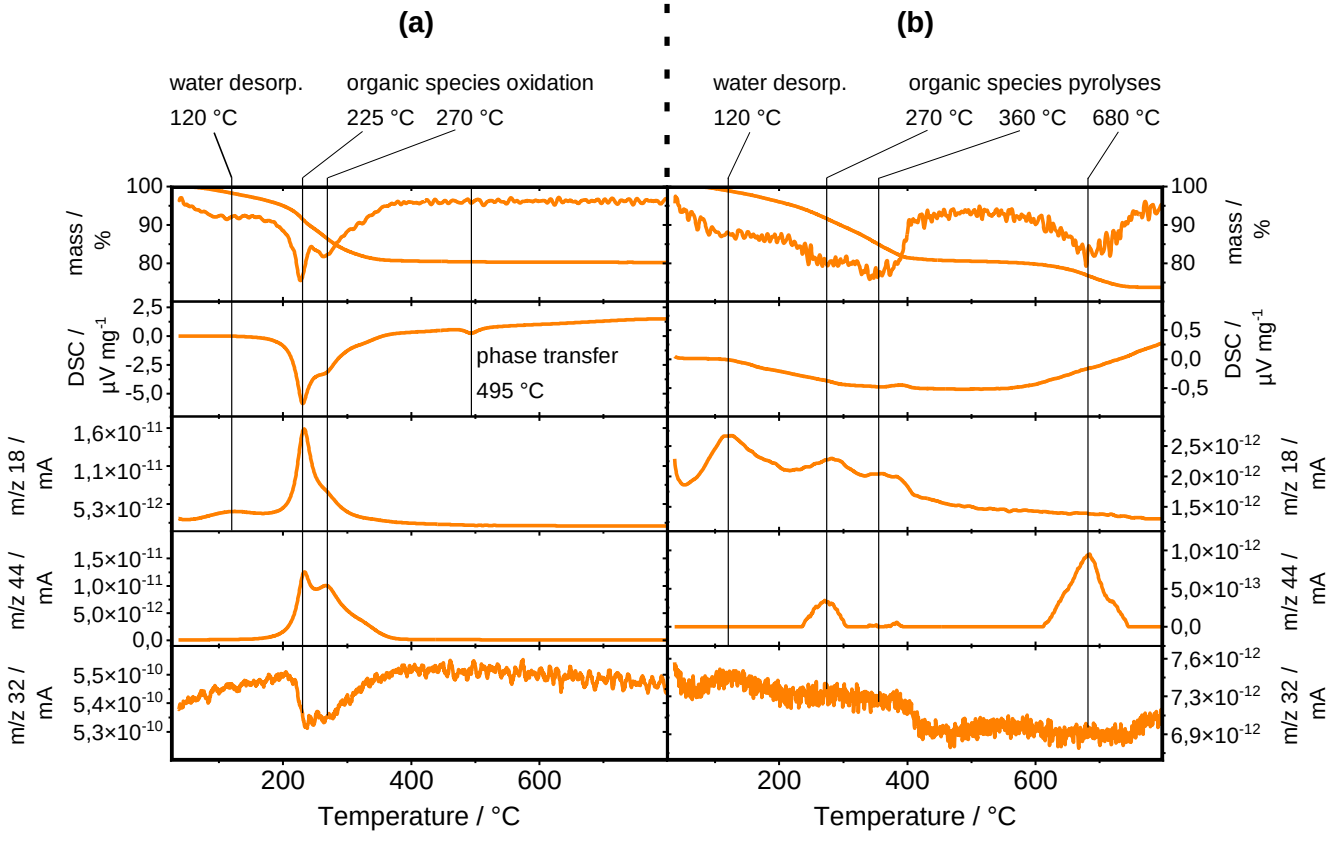

Figure 8: TGA-DSC-MS measurements for maghemite samples made by SpraySyn and using 0.1 M INN in EtOH and 2-EHA in air **(a)** and argon **(b)** gas atmosphere.

The data for treatment in air is shown in panel **(a)**. In this atmosphere, initially, the sample exhibited mass loss accompanied by water emission below ~200 °C. Since no significant signals other than m/z 18 were observed in this temperature range and the DSC showed a slight positive curvature (weak endothermic event), the water release was attributed to physical water desorption, with the desorption maximum at 120 °C. In the subsequent temperature range (>200 °C), the m/z 18 signal showed strong maxima coinciding with exothermic DSC signals. Those events were accompanied by m/z 44 (CO_2) maxima as well as m/z 32 (O_2) minima. The corresponding maxima ware identified at 227 and 273 °C (marked by lines in **Figure 8**). Those

https://doi.org/10.5194/ar-2023-14
Preprint. Discussion started: 3 November 2023

events indicated presence of organic species, and it is evident that these species undergo oxidation in the medium temperature range, resulting in the emission of CO_2/H_2O and consumption of O_2. Hence, TGA-DSC-MS is qualitatively consistent with the ATR-FTIR analysis. The evolution of the relative mass exhibited a sigmoidal shape due to the surface adsorbates oxidation, reaching steady state at ~400 °C in air. As also shown in **(a)** a further exothermic event was observed at around 490 °C, corresponding to the phase transformation of the particle phase from maghemite to hematite (Schwertmann und Cornell 2008; Cornell et al. 2003). Samples were also exposed to argon **(b)** to investigate their thermal behavior under oxygen restriction. Similar to the air experiment, the m/z 18 signal exhibited maxima at approximately 120 °C due to water desorption. However, in contrast to the air treatment, more CO_2/H_2O maxima were observed over a wider temperature range. Obviously, the oxygen restriction led to pyrolysis, resulting in the split of thermal events. Hence, the oxidation of organics was hindered by the absence of oxygen. And in contrast to air, in argon CO_2 and H_2O signals displayed four maxima at 273, 354, 385, and 690 °C, respectively. In summary, the TGA-DSC measurements showed that the particle surface can be purified stepwise by increasing the temperature. The purification is much more efficient in air. Thus, the data indicates that particle samples can be purified by thermal annealing in a mild temperature range of 200-300°C in air.

3.1.3 Carbonate und carboxylate quantification

As mentioned, samples prepared from precursor solutions containing different precursor concentrations showed qualitatively identical behavior during TGA-DSC-MS but differed quantitatively. The quantitative differences in the thermal behavior of both samples are shown in **Table 6**. There it is presented that the mass loss of the sample derived from using 0.1 M INN in the precursor solution was much higher than the sample from 0.2 M INN. This fact indicated already at first glance, that the impurities are mainly present on the particle surface, so that the impurity amount scales with the specific surface area of the powder. Additionally, mass losses in argon were higher than under air. This observation suggests that oxygen from the particle phase was utilized for the oxidation of organic surface species during TGA-MS-DSC. As the impurities were expected to be present as surface adsorbates, we calculated the mass loss caused by the oxidation of organics in air (150 °C<T<400 °C) and we related those values to the samples BET specific surface area (S_A). This normalization method aimed to derive a value for the particle surface loading density (unit: mg m^{-2}). Interestingly, the samples derived from both precursor solutions attained nearly identical values this way (0.85 and 0.84 mg m^{-2}). By assuming that the change in the INN concentration does not affect the flame chemistry and the evolution of impurities significantly, the normalization supports the claim that contaminant species are dominantly present on the particle surface. The mass losses caused by physical water desorption from the particle surface (20 °C<T<150 °C) were also calculated and related to S_A. This way, almost identical values were derived for the water presence (0.14 mg m^{-2}) for both samples.

https://doi.org/10.5194/ar-2023-14
Preprint. Discussion started: 3 November 2023

Table 6: Relation of mass losses determined by TGA-DSC-MS to the BET specific surface area (S_A). Mass losses were either caused by oxidation of organics (bound on particle surfaces) or by physical water desorption. The amount of water and organics can be normalized to S_A.

INN concentration	**0.1 M**	**0.2 M**
total mass losses during TGA		
air / %	19.80	17.01
argon / %	26.23	22.79
relation of mass losses during air treatment to S_A		
water relative mass: (m(50°C)-m(150°C))/m(50°C) / %	2.70	2.43
relating the water relative mass to S_A / mg m^{-2}	0.14	0.14
organic relative mass: (m(150°C)- m(400°C))/m(50°C) / %	16.67	14.12
relating the organic relative mass to S_A / mg m^{-2}	**0.85**	**0.84**

3.2 TS-TEM

In our second experimental approach, samples were extracted from the process by thermophoretic sampling (TS) and the corresponding particle ensembles were investigated by TEM with respect to structure and purity. The focus of this experiment was on the detection of carbon as impurity. Two positions were chosen for TS extraction, namely 5 cm and 15 cm *HAB*, representing very interesting positions for TS-TEM investigations. The position 5 cm *HAB* represents the center of the visible flame as already shown in **Figure 2**. For this position it can be assumed that the particle formation, which is dominated by agglomeration and sintering within the flame due to the high temperatures, is not completed so far (Fröde et al. 2023). It is also important to know that a droplet phase is still present at this position for the setup used (Karaminejad et al. 2023), so that the evaporation of precursor and solvent and reactions in the gas phase take place here simultaneously. The 15 cm position is about 7 cm above the visible flame tip. In a simplified numerical model, Fröde et al. showed that at this position the aerosol temperature is already strongly reduced, so that primary particle growth via sintering mechanisms is already considerably restricted there (Fröde et al. 2023; Tischendorf et al. 2021). Hence, particles extracted at 15 cm HAB roughly represent *final* particle structures. At these two positions, samples were extracted at different t_s values. The aim was to achieve lowest possible particle loadings to investigate single, individual agglomerates and aggregates.

3.2.1 Evaluating particle characteristics at 15 cm *HAB*

Initially, particles were extracted at 15 cm *HAB*, the position where primary particle growth by agglomeration and sintering is almost complete. For this purpose, a sampling time with t_s=100 ms was used (by exposing a TEM grid several times). **Figure 9 (a)** shows characteristic illustrations of this sample. As shown in panel 1, individual fine agglomerates and aggregates were scattered over the grid. As shown, the spatial particle distribution was generally uniform. At first glance, particles of a few tens of nanometers appeared to be present. Numerous particles were magnified, and some of them are shown as examples in panels 2-5. It was observed that fabricated particles were rather compact in structure. For example, panel 2 shows an aggregate, which consisted of only a few large primary particles, and thus, did not exhibit a fractal structure. Such structures were

https://doi.org/10.5194/ar-2023-14
Preprint. Discussion started: 3 November 2023

dominantly present. The particle examples in panels 3 and 4 showed even more compact structures (with panel 4 presenting a hexagonal single particle without any agglomeration/aggregation). To illustrate the representativeness of the aggregates and agglomerates shown, the particle size distribution at the identical sampling position is shown in **(b)**. Note, the size distribution was obtained via scanning mobility particle sizing (SMPS) by extracting an aerosol sample at the 15 cm *HAB* position via a hole in a tube (HIAT) probe (Tischendorf et al. 2021). As proven by HIAT-SMPS, the particle sizes (i.e., equivalent mobility diameter of aggregates) were dominantly in the size range of ~5-25 nm, which is in good accordance to the TEM illustrations. In this regard, the mean size of the particle ensemble attained $d_{P,EM}$=10.5 nm and a distribution width of $\sigma_{G,N}$=1.51. Going back to **(a)**, we observed that all particles showed pronounced crystal plane diffractions, and no indications for amorphous structures/coatings were found. Some small particles appeared amorphous at first glance (see small particle in the upper right of panel 4). However, when magnified (panel 5), crystal plane diffractions were clearly visible. In terms of the soot-detection TS-TEM investigations were in absolute agreement to TEM examinations made on the final powder product.

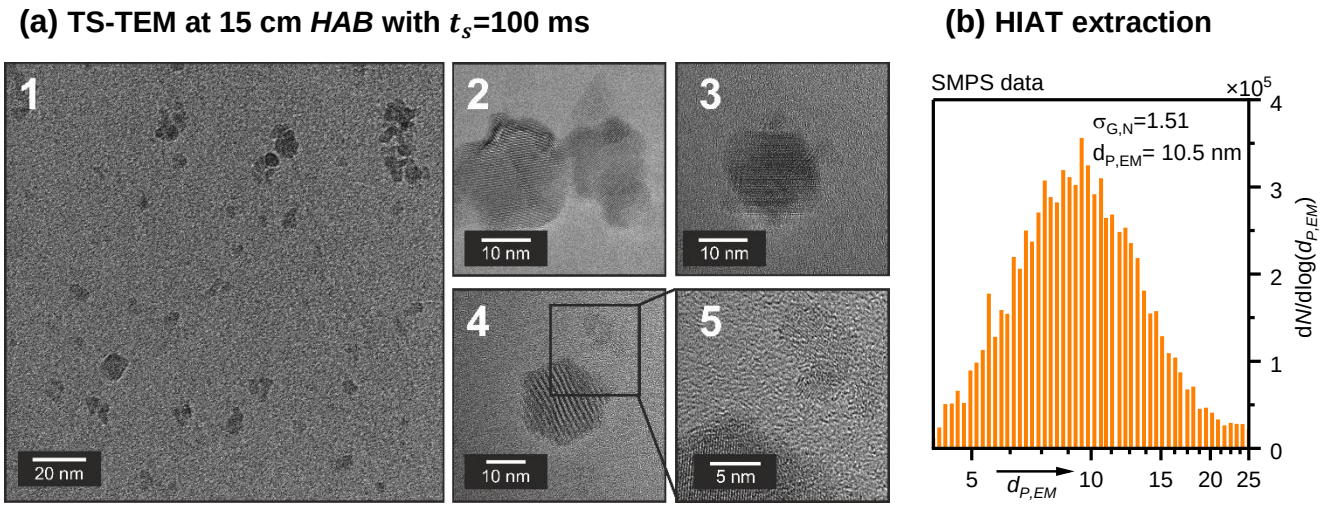

Figure 9: Size and morphology of iron oxide particles collected at 15 cm *HAB* using SpraySyn and 0.1 M INN in EtOH and 2-EHA. **(a)**: illustrations of typical particle structures obtained by TS. **(b)**: The corresponding mobility size distribution measured by SMPS after sampling by means of a hole in a tube (HIAT) probe. With $d_{P,EM}$ as electrical mobility equivalent diameter, N as number concentration, and $\sigma_{G,N}$ as number-weighted distribution width.

3.2.2 Evaluating particle characteristics at 5 cm *HAB*

At 5 cm *HAB*, particles were extracted from the center of the visible flame, a position where mixture formation, ignition, and evaporation of precursor components take place. As it was assumed that a much higher temperature would be present at this position compared to 15 cm *HAB*, shorter sampling times were used. Initially, samples were therefore extracted using t_s=40 ms and the corresponding TEM illustrations are shown in **Figure 10**. Under low magnification (panel 1), it quickly became apparent that thermal decomposition of the grid occurred despite t_s was reduced. At this point, it must be briefly explained that a TEM grid consists of a metallic mesh backbone covered by a thin carbon film. In panel 1, therefore, it can be seen that

https://doi.org/10.5194/ar-2023-14
Preprint. Discussion started: 3 November 2023

most of the carbon film has been decomposed. And as illustrated, only a few fragments of the film remained in the corners of the mesh. Examination of the particles in these heavily impacted areas showed that very high particle loadings were obtained (see the dense arrangement of particles in panels 2 and 3). Additionally, interestingly, several amorphous structures were found. Those structures can be seen on panels 4-8. Here, 4 and 5 show two images under lower magnification, and some core-shell structures are highlighted with asterisks. The panels 6, 7, and 8 show some of those particles under higher magnification allowing a clearer visualization. As shown, the outer shells which have been amorphous were clearly distinguishable from inner crystalline particle cores. The presence of these hetero-structures indicated the presence of amorphous carbon present as thin layer on particle surfaces.

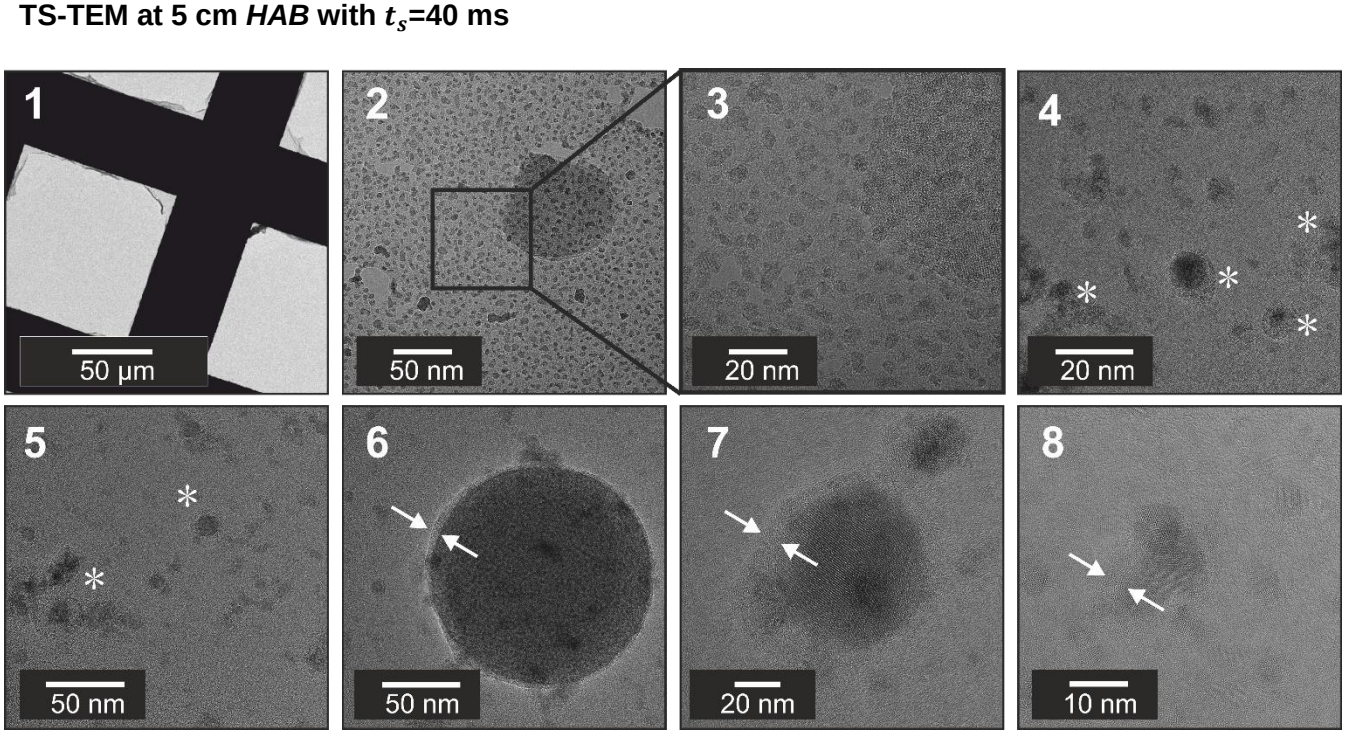

Figure 10: Results from TS-TEM experiments at 5 cm *HAB* using $\mathbf{t_s}$ = 40 ms exposure time and SpraySyn with 0.1 M INN in EtOH and 2-EHA as precursor composition.

Since it was not excluded that the partial grid oxidation/decomposition which took place at 40 ms could have contributed to the formation of carbon layers, further samples were subsequently extracted at a much lower t_s value. Hence a very short sampling time of 1.5 ms was applied. To relate the sample extraction to flame pulses, which take place on the same timescale (Karaminejad et al. 2023; Bieber et al. 2021) the sampling process was monitored using a high-speed camera. Two samples were subsequently selected for TEM analysis: The first sample had been extracted at a time between two flame pulsations, while the second sample was taken during a strong flame pulse. It should be emphasized that although the flame activity is

https://doi.org/10.5194/ar-2023-14
Preprint. Discussion started: 3 November 2023

significantly reduced in the interval between pulses, it does not drop to zero. In the literature, this flame state is also referred to as flame flickering (Bieber et al. 2021). **Figure 11** shows some exemplary TEM images of the flickering sample **(a)** compared with particle structures of the pulse sample **(b)**. The comparison of the samples by TEM showed clear differences with regard to the presence of amorphous structures. Thus, no amorphous layers or amorphous individual particles were found in the flickering sample, even after an intensive search. Instead, all particles were distinctly crystalline. On this sample, numerous aggregates were found (panels 2, 3, 7), non-aggregated single particles (5), and large-scale particles which probably originated from the droplet synthesis pathway (4). As shown in magnification (6 and 7), particles exhibited a high crystallinity and clean surfaces.

https://doi.org/10.5194/ar-2023-14
Preprint. Discussion started: 3 November 2023

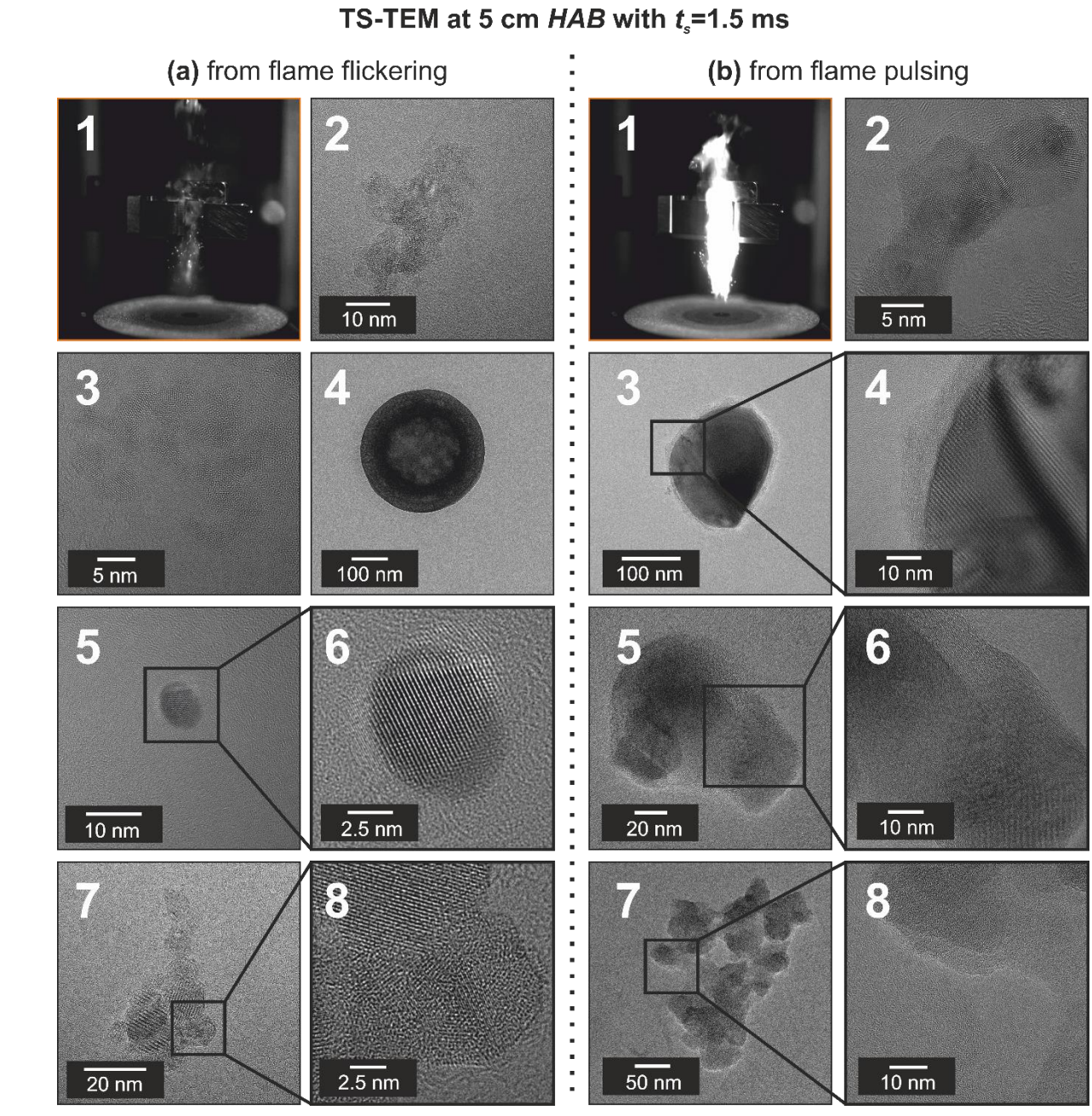

Figure 11: Results from TS-TEM experiments at 5 cm *HAB* using $\mathbf{t_s}$ = 1.5 ms exposure time and SpraySyn with 0.1 M INN in EtOH and 2-EHA as precursor composition during a) flickering (i.e. period of low flame activity) and b) flame pulsing (i.e. temporarily high flame activity).

In contrast, the pulse sample as shown in **(b)** exhibited strongly pronounced impurities in the form of amorphous structures. Although aggregates were also found which were exclusively crystalline (panel 2), the grid was showing multiple core-shell type particles (3, 4). Magnification of the edge regions of the particles showed, analogous to the 40 ms sample, that outer shells

https://doi.org/10.5194/ar-2023-14
Preprint. Discussion started: 3 November 2023

were amorphous, while inner cores were crystalline. Some of the outer layers showed also C-onion structures typical for elementary carbon depositions (6). In addition, a few aggregates were found which were completely amorphous (see the aggregate in panel 7 and the magnification in 8).

3.2.3 Relation of TS-TEM experiments

In summary, the TS-TEM experiments have shown that a solid, amorphous phase forms in the visible flame at 5 cm *HAB*. This phase coexists with the highly crystalline particle phase and forms both amorphous individual agglomerates and particle shells. Apparently, the formation of this phase appears during flame pulsations (i.e. high flame activity) rather than during flame flickering. One possible explanation for our observations could be the formation of soot/graphite. The interesting fact that both, the final powder product and TS-TEM samples extracted at 15 cm *HAB*, were microscopically pure (i.e., do not exhibit any of these amorphous structures) suggests that this contamination oxidizes downstream of 5 cm *HAB*. From physical perspective a presence/evolution of soot within pulsations indicate locally rich conditions (oxygen deficiency). The core-shell particle structures in our study are qualitatively comparable to TEM images of carbon-coated iron oxides known from literature, e.g., as shown by Hermann et al. (Herrmann et al. 2009), Li et al. (Li et al. 2013), and Carjaval et al. (Carvajal et al. 2020). As mentioned by Li et al. iron-based SFS materials may tend to form carbon shells due to the carbon-catalytic property of iron. Some of the coatings examined in our study exhibited C-onion structures, which are typical of elementary carbon. The possibility that the observed amorphous structures could show solvent components (EtOH, 2-EHA) is excluded, as those species would evaporate in the vacuum of the TEM instrument. It is noteworthy to mention that TS-TEM experiments are always subjected to a certain experimental bias caused by the TS principle (a temperature gradient must exist between the TEM grid and the gas phase). In this consequence particles experience cooling during their thermophoretic motion which may favor the formation of carbon on particle surfaces. Hence, we suggest evaluating and quantifying the presence of soot in this SFS setup using further experimental and numerical techniques in future.

4 Study Conclusion

In our study, we investigated whether the formation of impurities (surface adsorbates and carbon/soot) takes place in the preparation of iron oxide particles using the SpraySyn laboratory burner and by utilizing established precursor compositions known from literature. The impurity formation was studied in two experimental approaches. In the first approach, powder samples generated at two different precursor compositions were collected downstream of the SFS and subsequently analyzed using complementary powder analytical techniques. It was found that maghemite was synthesized dominantly with average BET primary particle sizes <10 nm. By TEM, no amorphous structures could be found which would have indicated carbon deposits, so that the powders were designated as pure by TEM microscopy. However, complementary ATR-FTIR measurements showed that organic species were still present in the powders in the form of carboxylates and carbonates. The relative mass fraction of these organic impurities was measured by TGA-DSC-MS. All samples exhibited high mass losses

https://doi.org/10.5194/ar-2023-14
Preprint. Discussion started: 3 November 2023

this way (double-digit %-range), caused by the oxidation of the organic species, and it was indicated that the majority of organics can be oxidized under air atmosphere in the temperature range of 200-300 °C. Hence, TGA-MS-DSC demonstrated that SFS-produced iron oxides can potentially be purified via thermal annealing using laboratory furnaces. As it was assumed from ATR-FTIR that carboxylates and carbonates were bound to the particle surfaces, values for impurity surface loadings were calculated. Therefore, we related the carboxylates/carbonates relative mass fractions to the respective powders' specific surface areas as measured by BET. Interestingly, the samples which have been prepared from precursor compositions including a different amount of precursor attained almost identical surface loading values (0.84-0.85 mg m^{-2}). Assuming that the change the precursor concentration has not altered the formation of carbonates and carboxylates, this confirms the theory that impurities are dominantly present on particle surfaces. And apparently, if impurities are exclusively present on surfaces, their relative mass content can be normalized to the particles specific surface area. This normalization approach could be used in the future to quantitatively compare/denote the purity of SFS made powders in sensitivity studies.

In our second experimental approach, particle samples were extracted from two *HAB* positions along the flame axis using a tailored thermophoretic sampler (TS) system and subsequently examined microscopically using TEM. TS-TEM experiments conducted at 15 cm *HAB* (a position where particle formation is almost completed) showed that particles were microscopically pure and highly crystalline. No amorphous structures indicating a contamination by elemental carbon were found at this position consistent with the powder analysis described before. Interestingly, TS-TEM at 5 cm *HAB* revealed a completely different picture. Numerous heterogeneous particle structures (particularly core-shell structures) were discovered using TS-TEM. In most cases, crystalline iron-oxide particles were coated with an amorphous layer of a few nanometers in thickness. By adjusting the sampling time down to 1.5 ms, particle samples were selectively extracted from either large flame pulsations or flame flickering. The comparison of those samples showed that amorphous structures could predominantly be extracted from flame pulsations which represent a reactive multiphase mixture of gas, droplets, and particles. Probably momentarily under-stoichiometric conditions yield a momentary formation of elemental carbon. The co-existence of carbon aside of maghemite particles is of relevance, as particle mechanisms and in situ diagnostics such as small-angle X-ray scattering (SAXS) and wide-angle light scattering (WALS) may be biased to certain extend. Therefore, we encourage the consideration of carbon in future experimental SFS studies. The qualitative findings from the TS-TEM experiments could be quantified and compared in the future using complementary non-intrusive optical measurement techniques since an experimental bias cannot be excluded due to the intrusive nature of the TS probe. In future approaches TS-TEM samples could additionally be analyzed using electron energy loss spectroscopy (EELS) to provide quantitative information about the elemental composition of the amorphous layers.

https://doi.org/10.5194/ar-2023-14
Preprint. Discussion started: 3 November 2023

AEROSOL Research Discussions

Data and sample availability

Further information about methodical details (burner handling, precursor composition preparation) and data provided (TEM illustrations, quantitative measurement data, highspeed recordings) will be available in an open source database (www.spraysyn.org). Powder samples are available on request.

https://doi.org/10.5194/ar-2023-14
Preprint. Discussion started: 3 November 2023

Author contributions

R. Tischendorf

- Development of the study design by literature research and preliminary work
- Manuscript preparation (writing, data illustration, extended literature study)
- General study administration (coordination of measurements and meetings/discussions)
- Interpretation and relation of particle data (Raman, BET, TEM, ATR-FTIR, TGA-DSC-MS)
- Development and characterization of the TS probing system
- Technical operator of TS-TEM experiments incl. highspeed-visualization

K. Duschik

- Technical operator of the TEM device (conducting FFT and HRTEM analysis, capturing images)
- Interpretation of TEM illustrations (focusing on the proof for particle crystallinity)

S. Dupont

- Development of the study design by literature research and preliminary work
- Providing supportive information regarding highspeed visualization

F. Fröde

- Development of the study design by literature research and preliminary work
- Manuscript preparation (adaption of the manuscript/text structure)

H. Pitsch

- PI (subproject number: Pl 368/19-1)
- Providing feedback concerning the study design and the data interpretation (focus on the gas phase chemistry, mixture formation, combustion)

R. Kneer

- PI (subproject number: KN 764/20-1)
- Providing feedback concerning the study design and the data interpretation (focus on the spray formation/characterization and highspeed visualization)

M. Schaper

- Providing feedback concerning the data interpretation (focus on the particle characterization by TEM)

H.-J. Schmid

- PI (subproject number: SCHM 1429/13-1)
- Providing feedback concerning the data interpretation (focus on the particle characterization, incl. TS-TEM sampling and powder analysis techniques)

https://doi.org/10.5194/ar-2023-14
Preprint. Discussion started: 3 November 2023

Conflict of interests

The authors declare that they have no conflict of interest.

https://doi.org/10.5194/ar-2023-14
Preprint. Discussion started: 3 November 2023

Acknowledgements

We kindly thank the DFG (German Research Foundation) for funding (grant number 375857587 including subproject numbers: SCHM 1429/13-1, KN 764/20-1, Pl 368/19-1).

https://doi.org/10.5194/ar-2023-14
Preprint. Discussion started: 3 November 2023

References

Abdelsamie, Abouelmagd; Chi, Cheng; Nanjaiah, Monika; Skenderović, Ivan; Suleiman, Samer; Thévenin, Dominique (2021): Direct numerical simulation of turbulent spray combustion in the spraysyn burner: impact of injector geometry. In: *Flow Turbul Combust* 106 (2), S. 453–469.

Abdelsamie, Abouelmagd; Kruis, Frank Einar; Wiggers, Hartmut; Thévenin, Dominique (2020): Nanoparticle Formation and Behavior in Turbulent Spray Flames Investigated by DNS. In: *Flow Turbul Combust* 105 (2), S. 497–516. DOI: 10.1007/s10494-020-00144-y.

Abdelsamie, Abouelmagd; Thévenin, Dominique (2019): On the behavior of spray combustion in a turbulent spatially-evolving jet investigated by direct numerical simulation. In: *Proc Combust Inst* 37 (2), S. 3373–3382.

Alkan, Baris; Medina, Danea; Landers, Joachim; Heidelmann, Markus; Hagemann, Ulrich; Salamon, Soma et al. (2020): Spray-Flame-Prepared LaCo 1– x Fe x O 3 Perovskite Nanoparticles as Active OER Catalysts: Influence of Fe Content and Low-Temperature Heating. In: *ChemElectroChem* 7 (12), S. 2564–2574. DOI: 10.1002/celc.201902051.

Altenhoff, Michael; Teige, Christian; Storch, Michael; Will, Stefan (2016): Novel electric thermophoretic sampling device with highly repeatable characteristics. In: *Rev Sci Instrum* 87 (12), S. 125108. DOI: 10.1063/1.4971988.

Angel, Steven; Neises, Julian; Dreyer, Maik; Friedel Ortega, Klaus; Behrens, Malte; Wang, Yuan et al. (2020): Spray-flame synthesis of La(Fe, Co)O 3 nano-perovskites from metal nitrates. In: *AIChE J* 66 (1). DOI: 10.1002/aic.16748.

Angel, Steven; Schneider, Florian; Apazeller, Sascha; Kaziur-Cegla, Wiebke; Schmidt, Torsten C.; Schulz, Christof; Wiggers, Hartmut (2021a): Spray-flame synthesis of LaMO3 (M= Mn, Fe, Co) perovskite nanomaterials: Effect of spray droplet size and esterification on particle size distribution. In: *Proceedings of the Combustion Institute* 38 (1), S. 1279–1287.

Angel, Steven; Tapia, Juan David; Gallego, Jaime; Hagemann, Ulrich; Wiggers, Hartmut (2021b): Spray-Flame Synthesis of LaMnO 3+δ Nanoparticles for Selective CO Oxidation (SELOX). In: *Energy Fuels* 35 (5), S. 4367–4376. DOI: 10.1021/acs.energyfuels.0c03659.

Arabi-Katbi, O. I.; Pratsinis, S. E.; Morrison Jr., P. W.; Megaridis, C. M. (2001): Monitoring the Flame Synthesis of TiO2 Particles by in-situ FTIR Spectroscopy and Thermophoretic Sampling. In: *Combust Flame* 124, S. 560–572.

Aßmann, Simon; Münsterjohann, Bettina; Huber, Franz J. T.; Will, Stefan (2020): Droplet sizing in spray flame synthesis using wide-angle light scattering (WALS). In: *Appl Phys B* 126 (5), S. 1–13.

Aßmann, Simon; Münsterjohann, Bettina; Huber, Franz J. T.; Will, Stefan (2021): In Situ Determination of Droplet and Nanoparticle Size Distributions in Spray Flame Synthesis by Wide-Angle Light Scattering (WALS). In: *Materials* 14 (21), S. 6698.

Bargar, John R.; Kubicki, James D.; Reitmeyer, Rebecca; Davis, James A. (2005): ATR-FTIR spectroscopic characterization of coexisting carbonate surface complexes on hematite. In: *Geochim Cosmochim Ac* 69 (6), S. 1527–1542. DOI: 10.1016/j.gca.2004.08.002.

https://doi.org/10.5194/ar-2023-14
Preprint. Discussion started: 3 November 2023

Bieber, M.; Al-Khatib, M.; Fröde, F.; Pitsch, H.; Reddemann, M. A.; Schmid, H. J. et al. (2021): Influence of angled dispersion gas on coaxial atomization, spray and flame formation in the context of spray-flame synthesis of nanoparticles. In: *Exp Fluids* 62 (5), S. 1–13.

Bierwirth, Malte; Olszok, Vinzent; Ganesan, Varun Aiyar; Poostforooshan, Jalal; Weber, Alfred P. (2021): Investigation of Particle Formation of Electrospray Flame Pyrolysis Using a Scanning Mobility Particle Sizer. In: *Chem Ing Tech* 93 (8), S. 1307–1315.

Brunauer, S.; Emmet, P. H.; Teller, E. (1938): Adsorption of Gases in Multimolecular Layers. In: *J Am Chem Soc* 60, S. 309–319.

Carbone, Francesco; Moslih, Sabrine; Gomez, Alessandro (2017): Probing gas-to-particle transition in a moderately sooting atmospheric pressure ethylene/air laminar premixed flame. Part II: Molecular clusters and nascent soot particle size distributions. In: *Combustion and Flame* 181, S. 329–341. DOI: 10.1016/j.combustflame.2017.02.021.

Carvajal, Luisa; Buitrago-Sierra, Robison; Santamaría, Alexander; Angel, Steven; Wiggers, Hartmut; Gallego, Jaime (2020): Effect of Spray Parameters in a Spray Flame Reactor During FexOy Nanoparticles Synthesis. In: *J Therm Spray Tech* 29 (3), S. 368–383. DOI: 10.1007/s11666-020-00991-1.

Chatterjee, J.; Haik, Y.; Chen, C.-J. (2003): Size dependent magnetic properties of iron oxide nanoparticles. In: *J Magn Magn Mater* 257, S. 113–118.

Cho, J. (1999): An experimental study of silica-based particle formation and growth in flame hydrolysis deposition process. Ph. D. thesis, Seoul National University.

Cho, J.; Choi, M. (2000): Determination of Number Density, Size and Morphology of Aggregates in Coflow Diffusion Flames Using Light Scattering and Local Sampling. In: *J Aerosol Sci* 31 (9), S. 1077–1095.

Choi, M.; Cho, J.; Kim, H. W. (1999): Measurements of Silica Aggregate Particle Growth Using Light Scattering and Thermophoretic Sampling in a Coflow Diffusion Flame. In: *J Nanopart Res* (1), S. 169–183.

Cornell, Rochelle M.; Schwertmann, Udo; others (2003): The iron oxides: structure, properties, reactions, occurrences, and uses: Wiley-vch Weinheim (664).

D'Alessio, A.; Barone, A. C.; Cau, R.; D'Anna, A.; Minutolo, P. (2005): Surface deposition and coagulation efficiency of combustion generated nanoparticles in the size range from 1 to 10nm. In: *Proc Combust Inst* 30 (2), S. 2595–2603. DOI: 10.1016/j.proci.2004.08.267.

Dar, M. Ibrahim; Shivashankar, S. A. (2014): Single crystalline magnetite, maghemite, and hematite nanoparticles with rich coercivity. In: *RSC Adv* 4 (8), S. 4105–4113. DOI: 10.1039/C3RA45457F.

Dobbins, R. A.; C. M. Megaridis (1987): Morphology of Flame-Generated Soot As Determined by Thermophoretic Sampling. In: *Langmuir* 3 (2), S. 254–259.

Faria, D. L. A. de; Silva, S. V.; Oliveira, M. T. de (1997): Raman Microspectroscopy of Some Iron Oxides and Oxyhydroxides. In: *J Raman Spectrosc* 28, S. 873–878.

https://doi.org/10.5194/ar-2023-14
Preprint. Discussion started: 3 November 2023

Foo, Cheau Tyan; Unterberger, Andreas; Martins, Fabio JWA; Prenting, Markus M.; Schulz, Christof; Mohri, Khadijeh (2022): Investigating spray flames for nanoparticle synthesis via tomographic imaging using multi-simultaneous measurements (TIMes) of emission. In: *Opt Express* 30 (9), S. 15524–15545.

Fröde, F.; Grenga, T.; Dupont, Sophie M.L.; Kneer, R.; Tischendorf, R.; Massopa, O. et al. (2023): Large Eddy Simulation of Iron Oxide Formation in a Laboratory Spray Flame.

German, Randall (2014): Sintering: from empirical observations to scientific principles: Butterworth-Heinemann.

Goudeli, Eirini; Gröhn, Arto J.; Pratsinis, Sotiris E. (2016): Sampling and dilution of nanoparticles at high temperature. In: *Aerosol Sci Technol* 50 (6), S. 591–604. DOI: 10.1080/02786826.2016.1168922.

Grimm, S.; Schulz, M.; Barth, S.; Müller, R. (1997a): Flame pyrolysis – a preparation route for ultrafine pure gamma-Fe2O3 powders and the control of their particle size and properties. In: *J Mater Sci* 32, S. 1083–1092.

Grimm, S.; Stelzner, T.; Leuthäußer, J.; Barth, S.; Heide, K. (1997b): Particle size effects on the thermal behaviour of maghemite synthesised by flame pyrolysis. In: *Thermochim Acta* 300, S. 141–148.

Gröhn, A. J.; Eggersdorfer, M. L.; Pratsinis, S. E.; Wegner, K. (2014a): On-line monitoring of primary and agglomerate particle dynamics. In: *J Aerosol Sci* 73, S. 1–13. DOI: 10.1016/j.jaerosci.2014.03.001.

Gröhn, Arto J.; Pratsinis, Sotiris E.; Sánchez-Ferrer, Antoni; Mezzenga, Raffaele; Wegner, Karsten (2014b): Scale-up of Nanoparticle Synthesis by Flame Spray Pyrolysis: The High-Temperature Particle Residence Time. In: *Ind. Eng. Chem. Res.* 53 (26), S. 10734–10742. DOI: 10.1021/ie501709s.

Gul, Saima; Khan, Sher Bahadar; Rehman, Inayat Ur; Khan, Murad Ali; Khan, M. I. (2019): A Comprehensive Review of Magnetic Nanomaterials Modern Day Theranostics. In: *Front Mater* 6, Artikel 179. DOI: 10.3389/fmats.2019.00179.

Gupta, Ajay Kumar; Gupta, Mona (2005): Synthesis and surface engineering of iron oxide nanoparticles for biomedical applications. In: *Biomaterials* 26 (18), S. 3995–4021. DOI: 10.1016/j.biomaterials.2004.10.012.

Hanesch, Monika (2009): Raman spectroscopy of iron oxides and (oxy)hydroxides at low laser power and possible applications in environmental magnetic studies. In: *Geophys J Int* 177 (3), S. 941–948. DOI: 10.1111/j.1365-246X.2009.04122.x.

Heidermann, Th.; Jander, H.; Wagner, H. Gg. (1999): Soot Particles in Presmixed C2H4-Air-Flmaes at High Pressures (P=30-70 Bar). In: *Phys Chem Chem Phys* (1), S. 3497–3502.

Herrmann, Inge K.; Grass, Robert N.; Mazunin, Dmitry; Stark, Wendelin J. (2009): Synthesis and Covalent Surface Functionalization of Nonoxidic Iron Core−Shell Nanomagnets. In: *Chem. Mater.* 21 (14), S. 3275–3281. DOI: 10.1021/cm900785u.

Hu, Bing; Koylu, Umit (2004): Size and Morphology of Soot Particulates Sampled from a Turbulent Nonpremixed Acetylene Flame. In: *Aerosol Sci Technol* 38 (10), S. 1009–1018. DOI: 10.1080/027868290519111.

Hu, Bing; Yang, Bo; Koylu, Umit O. (2003): Soot measurements at the axis of an ethylene/air non-premixed turbulent jet flame. In: *Combust Flame* 134 (1-2), S. 93–106. DOI: 10.1016/S0010-2180(03)00085-3.

https://doi.org/10.5194/ar-2023-14
Preprint. Discussion started: 3 November 2023

Huber, Dale L. (2005): Synthesis, properties, and applications of iron nanoparticles. In: *Small* 1 (5), S. 482–501. DOI: 10.1002/smll.200500006.

Hung, C-H.; Katz, J. L. (1992): Formation of Mixed Oxide Powders in Flames: Part 1: TiO2-SiO2. In: *J Mater Res* 7 (7), S. 1861–1869.

Hurd, A. J.; Flowder, W. L. (1988): In Situ Growth and Structure of Fractal Silica Aggregates in a Flame. In: *J. Colloid Interface Sci.* 122 (1), S. 178–191.

Huu Do, Bao Phuong; Nguyen, Ba Dung; Nguyen, Hoang Duy; Nguyen, Phuong Tung (2013): Synthesis of magnetic composite nanoparticles enveloped in copolymers specified for scale inhibition application. In: *Adv Nat Sci* 4 (4), S. 45016. DOI: 10.1088/2043-6262/4/4/045016.

Ifeacho, Pascal; Huelser, Tim; Wiggers, Hartmut; Schulz, Christof; Roth, Paul (2007): Synthesis of SnO2−x nanoparticles tuned between 0⩽x⩽1 in a premixed low pressure H2/O2/Ar flame. In: *Proc Combust Inst* 31 (2), S. 1805–1812. DOI: 10.1016/j.proci.2006.07.083.

J. Cai/N. Lu/C. M. Sorensen (1993): Comparison of size and morphology of soot aggregates as determined by light scattering and electron microscope analysis. In: *Langmuir* 9, S. 2861–2867.

Janzen, C.; Kleinwechter, H.; Knipping, J.; Wiggers, H.; Roth, P. (2002): Size analysis in low-pressure nanoparticle reactors: comparison of particle mass spectrometry with in situprobing transmission electron microscopy. In: *J Aerosol Sci* 33, S. 833–841.

Jossen, R.; Pratsinis, S. E.; Stark, W. J.; Madler, L. (2005): Criteria for Flame-Spray Synthesis of Hollow, Shell-Like, or Inhomogeneous Oxides. In: *J Am Ceram Soc* 88 (6), S. 1388–1393. DOI: 10.1111/j.1551-2916.2005.00249.x.

Jubb, Aaron M.; Allen, Heather C. (2010): Vibrational Spectroscopic Characterization of Hematite, Maghemite, and Magnetite Thin Films Produced by Vapor Deposition. In: *ACS Appl Mater Interfaces* 2 (10), S. 2804–2812. DOI: 10.1021/am1004943.

Kammler, Hendrik K.; Beaucage, Gregory; Kohls, Douglas J.; Agashe, Nikhil; Ilavsky, Jan (2005): Monitoring simultaneously the growth of nanoparticles and aggregates by in situ ultra-small-angle x-ray scattering. In: *J Appl Phys* 97 (5), S. 54309. DOI: 10.1063/1.1855391.

Kammler, Hendrik K.; Jossen, Rainer; Morrison, Philip W.; Pratsinis, Sotiris E.; Beaucage, Gregory (2003): The effect of external electric fields during flame synthesis of titania. In: *Powder Technol* 135-136, S. 310–320. DOI: 10.1016/j.powtec.2003.08.023.

Kammler, Hendrik Klaus (2002): Synthesis of oxide nanoparticles with closely controlled characteristics. ETH Zurich.

Karaminejad, Sadrollah; Dupont, Sophie M.L.; Bieber, Malte; Reddemann, Manuel A.; Kneer, Reinhold; Dreier, Thomas et al. (2023): Characterization of spray parameters and flame stability in two modified nozzle configurations of the SpraySyn burner. In: *Proceedings of the Combustion Institute* 39 (2), S. 2673–2682. DOI: 10.1016/j.proci.2022.07.248.

https://doi.org/10.5194/ar-2023-14
Preprint. Discussion started: 3 November 2023

Keller, Alexander; Wlokas, Irenäus; Kohns, Maximilian; Hasse, Hans (2020): Thermophysical properties of solutions of Iron (III) nitrate-nonahydrate in mixtures of ethanol and water. In: *J Chem Eng Data* 65 (7), S. 3519–3527.

Kirchmann, J.; Kronenburg, A.; Stein, O. T.; Cleary, M. J. (2021): Two-phase sparse-Lagrangian MMC-LES of dilute ethanol spray flames. In: *Proc Combust Inst* 38 (2), S. 3343–3350.

Kotalczyk, Gregor; Skenderović, Ivan; Kruis, Frank Einar (2019): Monte Carlo simulations of homogeneous nucleation and particle growth in the presence of background particles. In: *Tellus B Chem Phys Meteorol* 71 (1), S. 1554415.

Kotalczyk, Gregor; Skenderović, Ivan; Kruis, Frank Einar (2022): Monte Carlo simulations of homogeneous nucleation and particle growth in the presence of background particles. In: *Tellus B Chem Phys Meteorol* 71 (1), S. 1554415. DOI: 10.1080/16000889.2018.1554415.

Koylu, U. O.; Faeth, G. M. (1992): Structure of Overfire Soot in Buoyant Turbulent Diffusion Flames at Long Residence Times. In: *Combust Flame* 89, S. 140–156.

Koylu, U. O.; McEnally, C. S.; Rosner, Daniel E.; Pfefferle, L. D. (1997): Simultaneous Measurements of Soot Volume Fraction and Particle Size / Microstructure in Flames Using a Thermophoretic Sampling Technique. In: *Combust Flame* 110, S. 494–507.

Koylu, U. O.; Xing, Y.; Rosner, Daniel E. (1995): Fractal Morphology Analysis of Combustion-Generated Aggregates Using Angular Light Scattering and Electron Microscope Images. In: *Langmuir* 11, S. 4848–4854.

Kruis, F. E.; Oostra, W.; Marijnissen, J.; Schoonman, J.; Scarlett, B. (1998): Particle Formation Paths in the Synthesis of Silicon Nitride Powder in a Laser-Heated Aerosol Reactor. In: *J Eur Ceram Soc* 18, S. 1025–1036.

Kumar, Abhijeet; Kirchmann, Jonas; Beyrau, Frank; Kronenburg, Andreas (2023): Jet flapping and its effect on flame oscillations in the SPP1980 SpraySyn burner. In: *Experimental Thermal and Fluid Science* 142, S. 110826. DOI: 10.1016/j.expthermflusci.2022.110826.

Kunze, Frederik; Kuns, Stefan; Spree, Mathias; Hülser, Tim; Schulz, Christof; Wiggers, Hartmut; Schnurre, Sophie M. (2019): Synthesis of silicon nanoparticles in a pilot-plant-scale microwave plasma reactor: Impact of flow rates and precursor concentration on the nanoparticle size and aggregation. In: *Powder Technol* 342, S. 880–886. DOI: 10.1016/j.powtec.2018.10.042.

Lapuerta, Magín; Martos, Francisco J.; Herreros, José M. (2007): Effect of engine operating conditions on the size of primary particles composing diesel soot agglomerates. In: *J Aerosol Sci* 38 (4), S. 455–466. DOI: 10.1016/j.jaerosci.2007.02.001.

Lee, D.; Choi, M. (2000): Control of Size and Morphology of Nona Particles Using CO2 Laser During Flame Synthesis. In: *J Aerosol Sci* 31 (10), S. 1145–1163.

Lee, Jeonghoon; Altman, Igor; Choi, Mansoo (2008a): Design of thermophoretic probe for precise particle sampling. In: *J Aerosol Sci* 39 (5), S. 418–431. DOI: 10.1016/j.jaerosci.2008.01.001.

https://doi.org/10.5194/ar-2023-14
Preprint. Discussion started: 3 November 2023

Lee, Yun-Jo; Jun, Ki-Won; Park, Jo-Yong; Potdar, Hari S.; Chikate, Rajeev C. (2008b): A simple chemical route for the synthesis of γ-Fe2O3 nano-particles dispersed in organic solvents via an iron–hydroxy oleate precursor. In: *J Ind Eng Chem* 14 (1), S. 38–44. DOI: 10.1016/j.jiec.2007.08.009.

Leschowski, M.; Dreier, T.; Schulz, C. (2014): An automated thermophoretic soot sampling device for laboratory-scale high-pressure flames. In: *Rev Sci Instrum* 85 (4), S. 45103. DOI: 10.1063/1.4868970.

Leschowski, Martin; Dreier, Thomas; Schulz, Christof (2015): A Standard Burner for High Pressure Laminar Premixed Flames: Detailed Soot Diagnostics. In: *Z Phys Chem* 229 (5), S. 781–805. DOI: 10.1515/zpch-2014-0631.

Li, Dan; Teoh, Wey Yang; Selomulya, Cordelia; Woodward, Robert C.; Munroe, Paul; Amal, Rose (2007): Insight into microstructural and magnetic properties of flame-made γ-Fe2O3 nanoparticles. In: *J Mater Chem* 17 (46), S. 4876. DOI: 10.1039/b711705a.

Li, Haipeng; Riefler, Norbert; Wriedt, T.; Mädler, Lutz (2021): Reference data set for three-dimensional measurements of double droplet combustion of p-xylene. In: *Proc Combust Inst* 38 (2), S. 3151–3158. Online verfügbar unter https://www.sciencedirect.com/science/article/abs/pii/S1540748920303898.

Li, Shuiqing; Ren, Yihua; Biswas, Pratim; Tse, Stephen D. (2016): Flame aerosol synthesis of nanostructured materials and functional devices: Processing, modeling, and diagnostics. In: *Prog Energy Combust Sci* 55, S. 1–59. DOI: 10.1016/j.pecs.2016.04.002.

Li, Yunfeng; Hu, Yanjie; Huang, Guangjian; Li, Chunzhong (2013): Metallic iron nanoparticles: Flame synthesis, characterization and magnetic properties. In: *Particuology* 11 (4), S. 460–467. DOI: 10.1016/j.partic.2012.10.008.

Ma, J.; Fletcher, T. H.; Webb, W. (1995): Thermophoretic Sampling of Coal-Derived SooT during Devolatization. In: *Energy Fuels* 9, S. 802–808.

Majewski, Peter; Thierry, Benjamin (2007): Functionalized Magnetite Nanoparticles—Synthesis, Properties, and Bio-Applications. In: *Crit Rev Solid State Mater Sci* 32 (3-4), S. 203–215. DOI: 10.1080/10408430701776680.

Martins, Fabio J. W. A.; Kirchmann, J.; Kronenburg, A.; Beyrau, Frank (2020): Experimental investigation of axisymmetric, turbulent, annular jets discharged through the nozzle of the SPP1980 SpraySyn burner under isothermal and reacting conditions. In: *Exp Therm Fluid Sci* 114.

Martins, Fabio J. W. A.; Kirchmann, Jonas; Kronenburg, Andreas; Beyrau, Frank (2021): Quantification and mitigation of PIV bias errors caused by intermittent particle seeding and particle lag by means of large eddy simulations. In: *Meas Sci Technol* 32 (10), S. 104006. DOI: 10.1088/1361-6501/ac07d9.

Megaridis, C. M.; Dobbins, R. A. (1990): Morphological Description of Flame-Generated Materials. In: *Combust Sci Technol* 71 (1-3), S. 95–109. DOI: 10.1080/00102209008951626.

Meierhofer, Florian; Li, Haipeng; Gockeln, Michael; Kun, Robert; Grieb, Tim; Rosenauer, Andreas et al. (2017): Screening Precursor-Solvent Combinations for Li4Ti5O12 Energy Storage Material Using Flame Spray Pyrolysis. In: *ACS Appl Mater Interfaces* 9 (43), S. 37760–37777. DOI: 10.1021/acsami.7b11435.

https://doi.org/10.5194/ar-2023-14
Preprint. Discussion started: 3 November 2023

Meierhofer, Florian; Mädler, Lutz; Fritsching, Udo (2020): Nanoparticle evolution in flame spray pyrolysis—Process design via experimental and computational analysis. In: *AIChE Journal* 66 (2), Artikel e16885. DOI: 10.1002/aic.16885.

Mikami, T.; Kamiya, H.; Masayuki, H. (1996): The machanism of defluidization of iron particles in a fluidized bed. In: *Powder Technol* 89, S. 231–238.

Mueller, Roger; Jossen, Rainer; Kammler, Hendrik K.; Pratsinis, Sotiris E.; Akhtar, M. Kamal (2004): Growth of zirconia particles made by flame spray pyrolysis. In: *AIChE J* 50 (12), S. 3085–3094. DOI: 10.1002/aic.10272.

Nanjaiah, Monika; Pilipodi-Best, Anita; Lalanne, Matthieu R.; Fjodorow, Peter; Schulz, Christof; Cheskis, Sergey et al. (2021): Experimental and numerical investigation of iron-doped flames: FeO formation and impact on flame temperature. In: *Proc Combust Inst* 38 (1), S. 1249–1257.

Neer, A.; Koylu, Umit O. (2006): Effect of operating conditions on the size, morphology, and concentration of submicrometer particulates emitted from a diesel engine. In: *Combust Flame* 146 (1-2), S. 142–154. DOI: 10.1016/j.combustflame.2006.04.003.

Oh, S. J.; Cook, D. C.; Townsend, H. E. (1998): Characterization of Iron Oxides Commonly Formed as Corrosion Products on Steel. In: *Hyperfine Interact* 112 (1-4), S. 59–66.

Oltmann, H.; Reimann, J.; Will, S. (2012): Single-shot measurement of soot aggregate sizes by wide-angle light scattering (WALS). In: *Appl Phys B* 106 (1), S. 171–183. DOI: 10.1007/s00340-011-4781-z.

Oltmann, Hergen; Reimann, Jörg; Will, Stefan (2010): Wide-angle light scattering (WALS) for soot aggregate characterization. In: *Combust Flame* 157 (3), S. 516–522. DOI: 10.1016/j.combustflame.2009.10.011.

Pankhurst, Q. A.; Conolly, J.; Jones, S. K.; Dobson, J. (2003): Applications of magnetic nanoparticles in biomedicine. In: *Appl Phys B* 36, R167–R181.

Prenting, Markus Michael; Bin Dzulfida, Muhammad Imran; Dreier, Thomas; Schulz, Christof (2020): Characterization of tracers for two-color laser-induced fluorescence liquid-phase temperature imaging in sprays. In: *Exp Fluids* 61 (3), S. 1–15.

Prenting, Markus Michael; Shilikhin, Maksim; Dreier, Thomas; Schulz, Christof; Endres, Torsten (2021): Characterization of tracers for two-color laser-induced fluorescence thermometry of liquid-phase temperature in ethanol, 2-ethylhexanoic-acid/ethanol mixtures, 1-butanol, and o-xylene. In: *Appl Opt* 60 (15), C98-C113.

Rahinov, Igor; Sellmann, Johannes; Lalanne, Matthieu R.; Nanjaiah, Monika; Dreier, Thomas; Cheskis, Sergey; Wlokas, Irenäus (2020): Insights into the mechanism of combustion synthesis of iron oxide nanoparticles gained by laser diagnostics, mass spectrometry, and numerical simulations: a mini-review. In: *Energy Fuels* 35 (1), S. 137–160.

Reimann, J.; Kuhlmann, S.-A.; Will, S. (2009): 2D aggregate sizing by combining laser-induced incandescence (LII) and elastic light scattering (ELS). In: *Appl Phys B* 96 (4), S. 583–592. DOI: 10.1007/s00340-009-3546-4.

Rémazeilles, C.; Refait, Ph. (2009): Fe(II) hydroxycarbonate Fe2(OH)2CO3 (chukanovite) as iron corrosion product: Synthesis and study by Fourier Transform Infrared Spectroscopy. In: *Polyhedron* 28 (4), S. 749–756. DOI: 10.1016/j.poly.2008.12.034.

https://doi.org/10.5194/ar-2023-14
Preprint. Discussion started: 3 November 2023

Rosenberger, T.; Skenderović, I.; Sellmann, J.; Wollny, P.; Levish, A.; Wlokas, I. et al. (2022): Determining the sintering kinetics of Fe and Fe x O y -Nanoparticles in a well-defined model flow reactor. In: *Aerosol Sci Technol* 56 (9), S. 833–846. DOI: 10.1080/02786826.2022.2089011.

Saber, Fathy; Abdelsamie, Abouelmagd; Sedrak, Momtaz (2022): Numerical investigation of particle spray size distribution in turbulent jet flow. In: *J Eng Res* 174, M19-M40.

Schneider, F.; Suleiman, S.; Menser, J.; Borukhovich, E.; Wlokas, I.; Kempf, A. et al. (2019): SpraySyn—A standardized burner configuration for nanoparticle synthesis in spray flames. In: *Rev Sci Instrum* 90 (8), S. 85108.

Schwertmann, Udo; Cornell, Rochelle M. (2008): Iron oxides in the laboratory: preparation and characterization: John Wiley & Sons.

Sellmann, J.; Wollny, P.; Baik, S-J; Suleiman, S.; Schneider, F.; Schulz, C. et al. (2022): LES of nanoparticle synthesis in the spraysyn burner: A comparison against experiments. In: *Powder Technol* 404, S. 117466.

Skenderović, Ivan; Kotalczyk, Gregor; Kruis, Frank Einar (2018): Dual population balance Monte Carlo simulation of particle synthesis by flame spray pyrolysis. In: *Processes* 6 (12), S. 253.

Sklute, Elizabeth C.; Kashyap, Srishti; Dyar, M. Darby; Holden, James F.; Tague, Thomas; Wang, Peng; Jaret, Steven J. (2018): Spectral and morphological characteristics of synthetic nanophase iron (oxyhydr)oxides. In: *Phys Chem Miner* 45 (1), S. 1–26. DOI: 10.1007/s00269-017-0897-y.

Sodipo, Bashiru Kayode; Aziz, Azlan Abdul (2016): Recent advances in synthesis and surface modification of superparamagnetic iron oxide nanoparticles with silica. In: *J Magn Magn Mater* 416, S. 275–291. DOI: 10.1016/j.jmmm.2016.05.019.

Sorensen, C. M.; Feke, G. D. (1996): The Morphology of Macroscopic Soot. In: *Aerosol Sci Technol* 25 (3), S. 328–337. DOI: 10.1080/02786829608965399.

Sorvali, Miika; Honkanen, Mari; Hyvärinen, Leo; Kuisma, Ritva; Larjo, Jussi; Mäkelä, Jyrki M. (2021): Crystallographic phase formation of iron oxide particles produced from iron nitrate by liquid flame spray with a dual oxygen flow. In: *Int Jnl Ceramic Engine & Sci* 3 (5), S. 227–236. DOI: 10.1002/ces2.10102.

Sorvali, Miika; Nikka, Markus; Juuti, Paxton; Honkanen, Mari; Salminen, Turkka; Hyvärinen, Leo; Mäkelä, Jyrki M. (2019): Controlling the phase of iron oxide nanoparticles fabricated from iron(III) nitrate by liquid flame spray. In: *Int Jnl Ceramic Engine & Sci* 1 (4), S. 194–205. DOI: 10.1002/ces2.10025.

Steele, W. V.; Chirico, R. D.; Knipmeyer, S. E.; Nguyen, A. (1997): Vapor Pressure, Heat Capacity, and Density along the Saturation Line, Measurements for Cyclohexanol, 2-Cyclohexen-1-one, 1,2-Dichloropropane, 1,4-Di- tert -butylbenzene, (±)-2-Ethylhexanoic Acid, 2-(Methylamino)ethanol, Perfluoro- n -heptane, and Sulfolane. In: *J. Chem. Eng. Data* 42 (6), S. 1021–1036. DOI: 10.1021/je9701036.

Stefanidis, Evangelos K.; Ebaugh, Thomas A.; Bliznakov, Stoyan; Bonville, Leonard J.; Maric, Radenka; Carbone, Francesco (2022): Laser diagnostics to characterize the in-flame growth of platinum nanoparticles manufactured by

https://doi.org/10.5194/ar-2023-14
Preprint. Discussion started: 3 November 2023

the reactive spray deposition technology. In: *Combustion and Flame* 246, S. 112412. DOI: 10.1016/j.combustflame.2022.112412.

Stodt, Malte F. B.; Gonchikzhapov, Munko; Kasper, Tina; Fritsching, Udo; Kiefer, Johannes (2019): Chemistry of iron nitrate-based precursor solutions for spray-flame synthesis. In: *Phys Chem Chem Phys* 21 (44), S. 24793–24801.

Strobel, Reto; Pratsinis, Sotiris E. (2007): Flame aerosol synthesis of smart nanostructured materials. In: *J Mater Chem* 17 (45), S. 4743. DOI: 10.1039/b711652g.

Strobel, Reto; Pratsinis, Sotiris E. (2009): Direct synthesis of maghemite, magnetite and wustite nanoparticles by flame spray pyrolysis. In: *Adv Powder Technol* 20 (2), S. 190–194. DOI: 10.1016/j.apt.2008.08.002.

Strobel, Reto; Pratsinis, Sotiris E. (2011): Effect of solvent composition on oxide morphology during flame spray pyrolysis of metal nitrates. In: *Phys Chem Chem Phys* 13 (20), S. 9246–9252. DOI: 10.1039/c0cp01416h.

Suleiman, Samer; Nanjaiah, Monika; Skenderovic, Ivan; Rosenberger, Thore; Kunze, Frederik; Wlokas, Irenaeus et al. (2021): Atmospheric-pressure particle mass spectrometer for investigating particle growth in spray flames. In: *J Aerosol Sci* 158, S. 105827.

Teoh, Wey Yang; Amal, Rose; Mädler, Lutz (2010): Flame spray pyrolysis: An enabling technology for nanoparticles design and fabrication. In: *Nanoscale* 2 (8), S. 1324–1347. DOI: 10.1039/c0nr00017e.

Tischendorf, R.; Simmler, M.; Weinberger, C.; Bieber, M.; Reddemann, M.; Fröde, F. et al. (2021): Examination of the evolution of iron oxide nanoparticles in flame spray pyrolysis by tailored in situ particle sampling techniques. In: *J Aerosol Sci* 154, S. 105722.

Tsantilis, Stavros; Kammler, Hendrik K.; Pratsinis, S. E. (2002): Population balance modeling of&ame synthesis of titania nanoparticles. In: *Chem Eng Sci* 57, S. 2139–2156.

Vargas, Alex M.; Gülder, Ömer L. (2016): A multi-probe thermophoretic soot sampling system for high-pressure diffusion flames. In: *Rev Sci Instrum* 87 (5), S. 55101. DOI: 10.1063/1.4947509.

Vargas, Alex M.; Gülder, Ömer L. (2017): Pressure dependence of primary soot particle size determined using thermophoretic sampling in laminar methane-air diffusion flames. In: *Proc Combust Inst* 36 (1), S. 975–984. DOI: 10.1016/j.proci.2016.05.023.

Wollny, Patrick; Angel, Steven; Wiggers, Hartmut; Kempf, Andreas M.; Wlokas, Irenaeus (2020): Multiscale simulation of the formation of platinum-particles on alumina nanoparticles in a spray flame experiment. In: *Fluids* 5 (4), S. 201.

Xing, Y.; Koylu, U. O.; Rosner, Daniel E. (1996): Synthesis and Restructuring of Inorganic Nano-Particles in Counterflow Diffision Flames. In: *Combust Flame* 107, S. 85–102.

Xing, Y., Koylu, U. Y.; Rosner, Daniel E. (1999): In situ light-scattering measurements of morphologically evolving flame-synthesized oxide nanoaggregates. In: *Appl Opt* 38, S. 2686–2697.

Zhang, J.; Megaridis, C. M. (1998): Soot Microstructure in Steady and Flickering Laminar Methane/Air Diffusion Flames. In: *Combust Flame* 112, S. 473–484.

https://doi.org/10.5194/ar-2023-14
Preprint. Discussion started: 3 November 2023

Zhu, H. J.; Hill R. H. (2002): The photochemical metal organic deposition of manganese oxide films from films of manganese(II) 2-ethylhexanoate: a mechanistic study. In: *J Non Cryst Solids* 311, S. 174–184.

https://doi.org/10.5194/ar-2023-14
Preprint. Discussion started: 3 November 2023

AEROSOL Research Discussions

Appendix

Table A 1: Reaction equations used for calculating SFS-relevant analytical parameter.

species			molar fluxes	oxidation reaction
liquid feed	INN	$Fe(NO_3)_3*9H_2O$	6.66 µmol s^{-1}	$4\ Fe(NO_3)_3 \rightarrow 2Fe_2O_3 + 15O_2 + 6N_2$
liquid feed	EtOH	C_2H_5OH	0.20 mmol s^{-1}	$C_8H_{16}O_2 + 11O_2 \rightarrow 8H_2O + 8CO_2$
liquid feed	2-EHA	$C_8H_{16}O_2$	0.14 mmol s^{-1}	$C_2H_5OH + 3\ O_2 \rightarrow 3H_2O + 2CO_2$
dispersion gas	Oxygen	O_2	7.44 mmol s^{-1}	-
pilot flame gas	Methane	CH_4	1.49 mmol s^{-1}	$CH_4 + 2O_2 \rightarrow 2H_2O + CO_2$
pilot flame gas	Oxygen	O_2	11.90 mmol s^{-1}	-

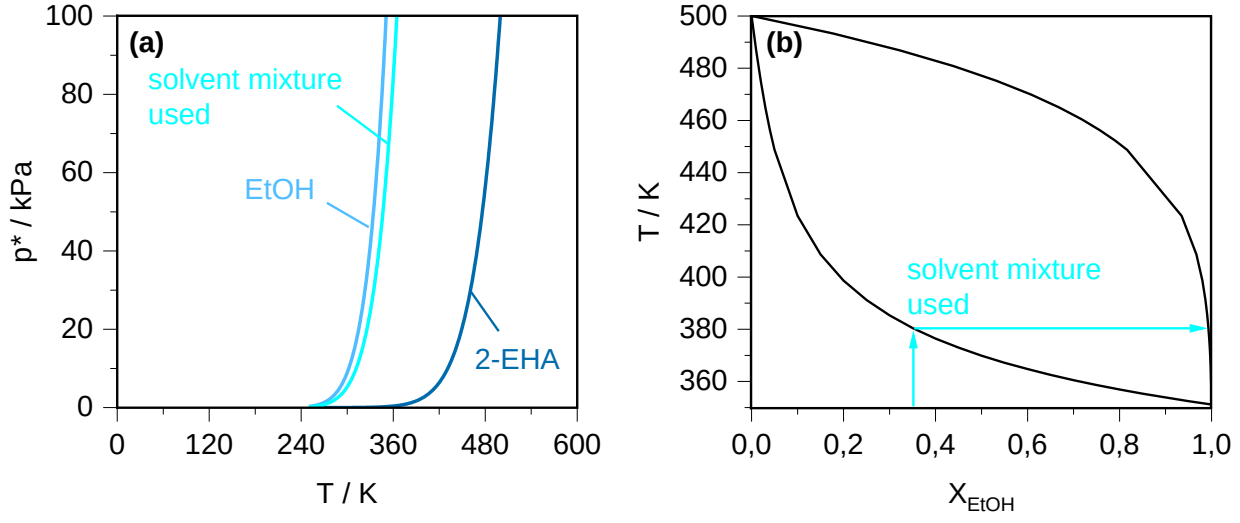

Figure A 1: Illustration of vapor pressure data for solvents EtOH and 2-EHA as well as their mixtures. With **(a)**: vapor pressure curves of pure EtOH, pure 2-EHA and the 35:65 mixture used in this study, and **(b)**: the boiling diagram of binary mixtures of EtOH and 2-EHA at atmospheric conditions. Note, vapor pressure data was taken from REFPROP (EtOH) and Steele et al. (2-EHA) (Steele et al. 1997). As visualized, due to the strongly different vapor pressure curves, EtOH should evaporates preferably *in situ*. Hence the characteristic parameter R_T as described by Jossen et al. should rise accordingly.

Table A 2: Comparison of experimental Raman vibrations to literature (most intense vibration **bold**, second underlined) in the wavenumber region <1000 cm^{-1}. Note, within this table, the reference peaks of different phases are ordered (each column contains peaks measured in a similar wavelength-regime and hence, the columns represent potential peak identifications for our experimental data. For instance: The experimental shoulder at 650 cm^{-1} could be explained by phonons of several phases.)

our sample:	*360*	*510*	*650*	***720***
γ-Fe_2O_3				
	T_{2g}	E_g		A_{1g}
1	365	511	-	**700**
2	350	512	665	**730**
3	381	486	670	**718**
4	350	500	-	**700**

https://doi.org/10.5194/ar-2023-14
Preprint. Discussion started: 3 November 2023

α-Fe_2O_3									
	A_{1g}	E_g	E_g	E_g	E_g	A_{1g}	E_g	LOE_U
5	229	249	**295**	302	414	500	615	660
6	226	-	**294**	-	408	493	608	663
7	225	245	**290**	-	407	491	608	654
2	225	245	**291**	-	411	500	611	661
4	225	247	**293**	299	412	498	613	-
3	226	245	**292**	-	411	497	612	-

Fe_3O_4			
	T_{2g}	E_g	A_{1g}
1	310	554	**672**
6	-	-	**670**
7	330	537	**663**
2	310	540	**670**
4	300	532	**661**
3	-	532	**667**

References here: 1: (Jubb und Allen 2010), 2:(Hanesch 2009), 3:(Oh et al. 1998), 4:(Faria et al. 1997), 5:(Sklute et al. 2018), 6:(Dar und Shivashankar 2014)